DEPARTMENT OF PHYSICS
UNIVERSITY OF JYVÄSKYLÄ
RESEARCH REPORT No. 6/2010

DENSITY FUNCTIONAL STUDIES OF THE ELECTRONIC STRUCTURE AND CATALYTIC PROPERTIES OF SMALL BARE AND LIGAND-PROTECTED GOLD CLUSTERS

BY
KATARZYNA ANNA KACPRZAK

Academic Dissertation
for the Degree of
Doctor of Philosophy

To be presented, by permission of the
Faculty of Mathematics and Natural Sciences
of the University of Jyväskylä,
for public examination in Auditorium FYS-1 of the
University of Jyväskylä on June 11, 2010
at 12 o'clock noon

Jyväskylä, Finland
June 2010

Preface

This work has been carried out during 2005 - 2010 in the Department of Physics and in the Nanoscience Center of the University of Jyväskylä.

I want to direct special thanks to my supervisor professor Hannu Häkkinen for his infinite patience, understanding and motivating guidance during my Ph.D. studies. I also would like to thank my co-supervisors: Dr Jaakko Akola for his collaboration and support specially in my very first publication **I** and Dr Olga Lopez-Acevedo for guidance and supervision in publications **II** and **III**. I am grateful to all of them for great advises and comments, which made possible for me to accomplish this thesis. I would like to also thank for very inspiring and successful work with Dr Henrik Grönbeck from the Competence Centre for Catalysis and Department of Applied Physics in the Chalmers Technical University, Göteborg, Sweden. I also appreciate motivating collaboration with Joseph Parker and professor Royce W. Murray from University of North Carolina at Chapel Hill, USA. I sincerely enjoyed scientific conversations with professor Eberhard K.U. Gross from Fritz-Haber-Institut Berlin, Germany and professor Robert van Leeuwen from Physics Department, Nanoscience Center, University of Jyväskylä, Finland. In addition, I would like to thank Dr Lauri Lehtovaara from Department of Applied Physics, Aalto University School of Science and Technology, Helsinki, Finland.

How sad would it be to live far from the family and home country without friends. I truly want to thank: Ewa and Maciek Włodarczyk, Kasia and Piotrek Zaczkowscy, Monika and Piotrek Prus, Agnieszka and Marcin Barabasz, Monika and Maciek Zgirscy, Noora Okkonen and Michał Szydłowski, Katia Liira and Teemu Nieminen, Jari Ylänne and Riitta-Liisa Kuittinen. In addition, I thank for nice out-of-science conversations during the lunch breaks: Ermelinda, Christine, Olga, Daniela, Rafael and Reza.

I am grateful for full support coming from Poland! Specially from Family and also friends from Kraków and Warszawa.

Finally, my greatest thanks go to my Husband Piotr and my Daughter Julia for bringing sunshine in the most difficult moments. I dedicate this thesis to them.

"Jeżeli ignorancja jest ciemnością umysłu, to wiedza jest jego światłem, a studiowanie i uprawianie nauki, choć wymagają nakładu sił i przezwyciężenia wielu słabości, są zanurzeniem się w świetle."

-Michał Heller "Jak być uczonym"

"If ignorance is darkness of mind, then knowledge is its light; studying and doing science, although it requires effort and conquering many weaknesses, is plunging into this light."

Abstract

In this thesis, bare and thiolate-protected gold nanoclusters and thiolated polymeric gold, silver and copper complexes are computationally studied by using density functional codes GPAW (grid projector augmented wave) and CPMD (Car-Parrinello molecular dynamics and metadynamics). Since 2007, breakthroughs in experimental structural determination of $Au_{25}(SR)_{18}^{-1}$ and $Au_{102}(SR)_{44}$ clusters (SR = thiolate) have revised the understanding of bonding motifs at the gold-sulfur nano-interface. The structure of both clusters can be written via a "Divide and Protect" structural motif as $Au_{Ncore}[Au_x(SR)_{x+1}]_y$ where a considerable number of Au atoms of the cluster are outside of the metal core, covalently bound with thiolates in the protective ligand layer. The Au_{25} cluster can be written as $Au_{13}[Au_2(SR)_3]_6^{-1}$ featuring an approximately icosahedral Au_{13} core and six oligomeric $Au_2(SR)_3$ units or "semi-rings". The comparative analysis of thiolated Cu, Ag, and Au complexes, related to the "semi-rings", shows that the metal-thiolate bond is sterically flexible, i.e., ring-like, helix-like or catenane-like complexes are energetically competitive for homoleptic complexes $(MeSM)_x$, where $x \leq 12$ (Me is methyl and M = Cu, Ag, Au). Among these complexes, the gold-thiolate bond is dominantly covalent with a slight electron charge transfer to sulfur and the copper-thiolate bond is most ionic among the three. The stability of the Au_{25} nanocluster can be understood from electron-shell-closing arguments. In its anionic form the cluster has 8 Au(6s) electrons in the metal core, composing a shell closing of P-type and rendering the cluster as a closed shell "superatom". Chemical modifications of the Au_{25} cluster was investigated by (i) replacing one Au atom by a Pd atom in the metal core or in the ligand shell, or by (ii) changing the nature of a simple methylthiolate ligand to more electronegative by chlorination. Both of these studies were motivated by experimental work and are helpful in interpreting the structural and electrochemical behaviour of doped clusters. The Au_{25} cluster, either in its all-gold or doped form, is a robust building block that could be used for designing cluster-based nanomaterials with tunable electronic, optical or magnetic properties. Finally, catalytic properties of (i) small, bare and neutral gold clusters (Au_2 and Au_4) for H_2O_2 formation and (ii) activated, partially thiolate-protected Au_{25} clusters for CO oxidation were studied. Reaction pathways for competing channels in H_2O_2 (hydrogen peroxide or water formation) were studied by room-temperature molecular dynamics and metadynamics. It was concluded that small gold clusters are fluxional (their structure can change during the reactions) and the size of the gold cluster can affect the probability of a given reaction channel. Activation of the Au_{25} cluster by partial removal of the protective layer changes the electron count in the metal core and renders the cluster an electropositive species that can bind molecular oxygen and produce CO_2 with considerably low (below 0.7 eV) activation barriers.

Author's address Katarzyna Anna Kacprzak
Department of Physics
University of Jyväskylä
Finland

Supervisor Professor Hannu Häkkinen
Department of Physics and
Department of Chemistry
University of Jyväskylä
Finland

Co-Supervisors Dr Jaakko Akola
Department of Physics
University of Jyväskylä
Finland

Dr Olga Lopez-Acevedo
Department of Physics
University of Jyväskylä
Finland

Reviewers Professor Martti Puska
Department of Applied Physics
Aalto University School of Science and
Technology
Espoo, Finland

Associate Professor Jakob Schiøtz
Department of Physics
Technical University of Denmark
Kongens Lyngby, Denmark

Opponent Assistant Professor Christine Aikens
Department of Chemistry
Kansas State University
Manhattan, KS, USA

List of Publications

I K. A. Kacprzak, J. Akola, and H. Häkkinen, *First-principles simulations of hydrogen peroxide formation catalyzed by small neutral gold clusters* Phys. Chem. Chem. Phys. **11**, 6359 (2009).

II K. A. Kacprzak, L. Lehtovaara, J. Akola, O. Lopez-Acevedo and H. Häkkinen, *A density functional investigation of thiolate-protected bimetal PdAu24(SR)(18)(z) clusters: doping the superatom complex* Phys. Chem. Chem. Phys. **11**, 7123 (2009) .

III O. Lopez-Acevedo, K.A. Kacprzak, J. Akola and H. Häkkinen, *Quantum size effects in ambient CO oxidation catalyzed by ligand-protected gold clusters* Nature Chem. **2**, 329 (2010)

IV J. Parker, K.A. Kacprzak, O. Lopez-Acevedo, H. Häkkinen, R.W.Murray, *An Experimental and Density Functional Theory Analysis of Serial Introductions of Electron-Withdrawing Ligands into the Ligand Shell of a Thiolate-Protected Au25 Nanoparticle* J. Phys. Chem. C, **114** (18), 8276 (2010)

V J. Akola, K.A. Kacprzak, O. Lopez-Acevedo, M. Walter, H. Grönbeck, H.Häkkinen, *Thiolate-protected Au25 superatoms as building blocks: dimers and crystals*, J. Phys. Chem. C ASAP, DOI: 10.1021/jp1015438

VI K.A. Kacprzak, O. Lopez-Acevedo, H.Häkkinen, H. Grönbeck, *Theoretical characterization of cyclic thiolated copper, silver and gold clusters*, submitted to J. Phys. Chem C

The author has done all of the numerical calculations in the publication **IV**, and part of it in the rest. The author has been conducting calculations and analysis as follows: in the **I** for catalysis on gold tetramer at 0 K and 300 K; in the **II** calculations excluding optical spectra; in the **III** for $Au_{25}(SMe)_{18}^{-1}$ system; in the **V** for dimeric undoped and doped $Au_{25}(SMe)_{18}^{-1}$; and in the **VI** calculations excluding non-stoichiometric complexes. The author has contributed writing all the publications. In addition, she wrote the first draft of the **VI** and the theory part for **IV**. Calculations were conducted using the density functional theory code CPMD (**I**) and GPAW (**II**, **III**, **IV**, **V** and **VI**). Furthermore, the author has contributed to the paper J.S. Hummelshøj et al., *"DFT based screening of ternary alkali-transition metal borohydrides - a computational materals design project"* J. Chem. Phys. **131**, 014101 (2009), which is excluded from the thesis.

Contents

List of Figures

1 Introduction

Gold. The chemical symbol for gold is Au and it derives from *aurum*, which means "shining dawn". It has an atomic number 79 and atomic weight 196.967 a.u. It is one of the elements which has an alchemical symbol: $\odot$. The first references dating back to 4000 B.C. describe gold as a fashion decorative objects used, what is today, in Eastern Europe and as money used by the Egyptians. However, only about 550 B.C. not weight of gold bars, but pureness of gold coins were introduced into the monetary system of Lydian Empire (now Turkey). Thus, the progression from a religious and artistic object to the invention of coinage was a condition *sine qua non* of human obsession over pieces of gold [1]. It is the most malleable and ductile metal with lustrous shine. In jewellery it is usually alloyed to give it more strength, and its purity is expressed in carats. Gold is very good conductor of heat and electricity, and it has a bright yellow color, but as finely divided, it is black and as a colloid its color ranges from ruby red to purple. Gold has the electronic configuration $[\mathrm{Xe}]4f^{14}5d^{10}6s^{1}$, and in bulk it is chemically inactive and it exhibits a face centered cubic atom-arrangement. In addition, bulk gold is unaffected by air and most reagents. However, when the size of gold particles decreases down to few atoms their properties change drastically due to their chemical and quantum mechanical properties. Particularly, investigation of gold nano-crystallites is interesting because they have been found to reveal unique size-dependent properties differing from those in bulk.

The transition of matter from the atomic regime to the solid state implies changes of matter aggregation, and various kinds of nano-objects exist, such as fullerenes, atomic clusters and inorganic nanocrystals with sizes of the order of 1-10 nm, and they display quantum behaviour and size-dependent properties. Synthesis of these systems motivates researchers and engineers to go beyond single nano-scale units and develop new materials from such systems. Hence, basic scientific research may make a desired connection between science and "real" life. However, the design of such materials with well defined properties is challenging. One research field studies clusters of atoms rather than single atoms [2, 3]. It is necessary to understand the elementary building blocks, such as single clusters, in order to predict and apprehend material properties. Clusters exhibit physical properties which are intermediate between atomic and bulk, and one can build material where they are ordered into superlattices with controlled properties, such as selection of the sizes and composition. This suggests their application as components in electronic, optoelectronic, and sensor technologies. In order to design cluster-assembled materials, it is important to develop sufficient approaches, which prevent aggregation of separated building blocks. Furthermore, the

choice of clusters that exhibit enhanced stability is significant. Such clusters may be called as "superatoms".

One type of these nano-objects are nanoparticles, the so-called monolayer protected clusters (MPC), which contain two parts: a core and stabilizing layer. When the diameter of the core is sufficiently small, the quantum confinement effect is observed and properties are different that in the bulk. On the other hand, the stabilizing shell prevents particles from aggregation and sintering. Typically, thiols are the standard way of passivating the surfaces of metal nanoparticles. Particularly, self-assembled, ligand stabilized gold nanoparticles have received considerable research attention over the last few years due to experimental single-crystal structure determinations [4, 5] of the exact structure of the anion $Au_{25}(S(CH_2)_2Ph)^-_{18}$ (Au25) and $Au_{102}(pMBA)_{44}$ (Au102, pMBA is para-mercaptobenzoic acid, SC_6H_4COOH) [6]. The structures reveal that a pair of thiolate groups together with a gold atom form a linear bridge between gold atoms of the uppermost layer of the core cluster. Before the breakthrough with the X-ray structure of Jadzinsky et al., researchers did not know that large atomic cluster, such $Au_{102}(pMBA)_{44}$, could attain "molecular" precision rather than being simply an arbitrary aggregate [7].

The properties, structure, and composition of the Au nanoparticle complexes depend on the degree of aggregation of the Au atoms, and they may be categorized into the following groups: Au(I)-thiolate polymers, gold nanocrystals protected by thiolate monolayers, and self-assembled monolayers (SAMs) on extended Au surfaces. The spectroscopic measurements of polymers and clusters disclose their optical and photophysical properties dependence on the core size and the number of thiolates, and their color ranges from transparent bright yellow to green or even black. Another important factor that affects the structures and photophysical properties of gold nano-complexes is the "aurophilic" interaction [8–10].

This thesis has two parts. The first begins with a background theory and computational implementation. Later, few of schemes which help to analyse results are introduced. The second part is related to results of the PhD studies, and it starts with the electronic structure and chemical properties of thiolated noble metal complexes, and the doping of thiolate-protected $Au_{25}(SR)^-_{18}$ cluster. Next, the $Au_{25}(SR)^-_{18}$ dimer is discussed as an example of potential application , and finally, the catalytic properties of small bare and thiolate-protected $Au_{25}(SR)^-_{18}$ clusters are studied. In the summary few challenging perspectives are presented.

2 Theory and Numerical Techniques

2.1 The Many-Body Hamiltonian

The Hamiltonian for a many-particle system with N electrons and M nuclei can be written as:

$$\hat{H} = \hat{T}_e + \hat{T}_n + \hat{V}_{ee} + \hat{V}_{en} + \hat{V}_{nn}, \tag{2.1}$$

where:

$$\hat{T}_e = -\sum_{i=1}^{N} \frac{\hbar^2}{2m_e} \nabla_i^2 \tag{2.2}$$

is the kinetic energy operator for the electrons,

$$\hat{T}_n = -\sum_{I=1}^{M} \frac{\hbar^2}{2m_I} \nabla_I^2 \tag{2.3}$$

is the kinetic energy operator for the nuclei,

$$\hat{V}_{ee} = \sum_{i=1}^{N} \sum_{j>i}^{N} \frac{e^2}{|\mathbf{r}_i - \mathbf{r}_j|} \tag{2.4}$$

is the electron-electron Coulomb interaction,

$$\hat{V}_{en} = -\sum_{i=1}^{N} \sum_{I=1}^{M} \frac{Z_I e^2}{|\mathbf{r}_i - \mathbf{R}_I|} \tag{2.5}$$

is the Coulomb potential acting on the electrons due to presence of the nuclei and

$$\hat{V}_{nn} = \sum_{I=1}^{M} \sum_{J>I}^{M} \frac{Z_I Z_J e^2}{|\mathbf{R}_I - \mathbf{R}_J|} \tag{2.6}$$

is the nucleus-nucleus Coulomb interaction. $\hbar$ is the Planck constant, m_e the mass of an electron, e the elementary charge, Z_I is the atomic number and m_I the mass of nucleus I. The coordinates of electrons and nuclei are denoted as $\mathbf{r}_i$ and $\mathbf{R}_I$, respectively.

The total energy is an expectation value of the Hamiltonian:

$$E[\Psi] = \langle \hat{H} \rangle = \frac{\langle \Psi | \hat{H} | \Psi \rangle}{\langle \Psi | \Psi \rangle} \tag{2.7}$$

with the ground state energy as:

$$E_0 = \min_{\Psi} E[\Psi]. \tag{2.8}$$

The many-body wave function $\Psi(\mathbf{r}, \mathbf{R})$ thus contains all the essential information on the system. In order to obtain practical solutions, a set of approximations has to be applied. One of the useful approximations concerns the way how the many-body wave function can be treated to separate the electronic and nuclear (ions) degrees of freedom, known as the Born-Oppenheimer approximation. It decouples the electronic and nuclear degrees of freedom due to the ratio of electronic to nuclear mass. Nuclei have much smaller velocities than electrons. Thus, the many-body complete wave function Ψ can be approximated as a product of electronic and nuclear parts $\tilde{\Psi}$:

$$\tilde{\Psi}(\mathbf{r}, \mathbf{R}) = \Psi_e(\mathbf{r}; \{\mathbf{R}\}) \Psi_n(\{\mathbf{R}\}), \tag{2.9}$$

where $\Psi_e(\mathbf{r}; \{\mathbf{R}\})$ is the electronic wave-function with the set of nuclear positions $\{\mathbf{R}\}$ as parameters. First the electronic equation is solved with the potential arising from fixed nuclei, and later the nuclei are moved as classical particles in the potential generated by the electrons. The kinetic energy operator for the nuclei can be discarded from equation (2.1) and the Hamiltonian operator becomes:

$$\hat{H}_{el} = -\sum_{i=1}^{N} \frac{\hbar^2}{2m_e} \nabla_i^2 + \sum_{i=1}^{N} \sum_{j>i}^{N} \frac{e^2}{|\mathbf{r}_i - \mathbf{r}_j|} + \hat{V}_{\mathbf{R}_I}^{ext}, \tag{2.10}$$

where $\hat{V}_{\mathbf{R}_I}^{ext}$ is the sum of potentials caused by electron-nuclear and nuclear-nuclear interactions. Thus, the main and not trivial task is to solve the Schrödinger equation for the electrons:

$$\hat{H}_{el} \tilde{\Psi} = E_{el} \tilde{\Psi}, \tag{2.11}$$

and later the nuclear-nuclear interaction energy can be added to get the total energy:

$$E = E_{el}(\{\mathbf{R}\}) + T_n + V_{nn}. \tag{2.12}$$

Traditional quantum-chemical computational methods are centered around solving $\tilde{\Psi}$ to the highest possible accuracy and calculating the necessary observables from it. The systems considered in this work have been solved by using another key theory of quantum chemistry and computational material science, which is based on using the *electron density* as the key variable containing all the information from a given system. This is the so-called Density Functional Theory (DFT) which is briefly discussed next.

2.2 The Density Functional Theory

2.2.1 The Hohenberg-Kohn Theorem

Already in the first half of the twentieth century Thomas (1927), Fermi (1927, 1928), Dirac (1930), and von Weiszäcker (1935) suggested diminishing degrees of freedom in the system, by expressing the ground state in terms of the particle density $n(\mathbf{r})$ instead of many-body wavefunction [11, 12]. In 1964, two scientists P. Hohenberg and W. Kohn published an article [13], in which they proved the existence of a unique mapping between an external potential $v[n](\mathbf{r})$ and the particle density $n(\mathbf{r})$ for a non-degenerate ground state, the potential being the functional of the density. This statement is known as the First Hohenberg-Kohn theorem. In addition, the Second Hohenberg-Kohn theorem states that it is possible to define a universal functional F[n] in terms of the density, which is independent on the external potential, and that the ground state energy is found by variational principle as a functional of the ground-state electron density:

$$E[n] = \langle \Psi | \hat{T} + \hat{U}^{el} + v_0(\mathbf{r}) | \Psi \rangle = F[n] + \int n(\mathbf{r}) v_0(\mathbf{r}) d^3r, \tag{2.13}$$

where $v_0(\mathbf{r})$ is a fixed external potential and $\hat{U}^{el}$ contains all electron-electron interactions.

The practical scheme to solve the equations was presented in the work of W. Kohn and L.J. Sham [14] in 1965. Walter Kohn received the Chemistry Nobel Prize in 1998 for his "development of density-functional theory"[15].

2.2.2 The Kohn-Sham Scheme

In 1965 Kohn and Sham [14] introduced a non-interacting single particle scheme to calculate the properties of the ground state of an N particle system. The key issue was to represent the quantum mechanical kinetic energy of the electrons, where earlier approximations had proven to be insufficient [11, 12]. The Kohn-Sham ansatz states, that an "auxiliary" system of N *non-interacting electrons* moving in an external local potential, called $v_s(r)$, which has the property that its many-body wavefunction - a single Slater determinant of the lowest N orbitals ψ_i - yields precisely the same electron density as the exact interacting electron system with potential $v(\mathbf{r})$. Hence, the ground state density of the many-body interacting system is equal to the ground state density of an auxiliary non-interacting independent particle system. The kinetic

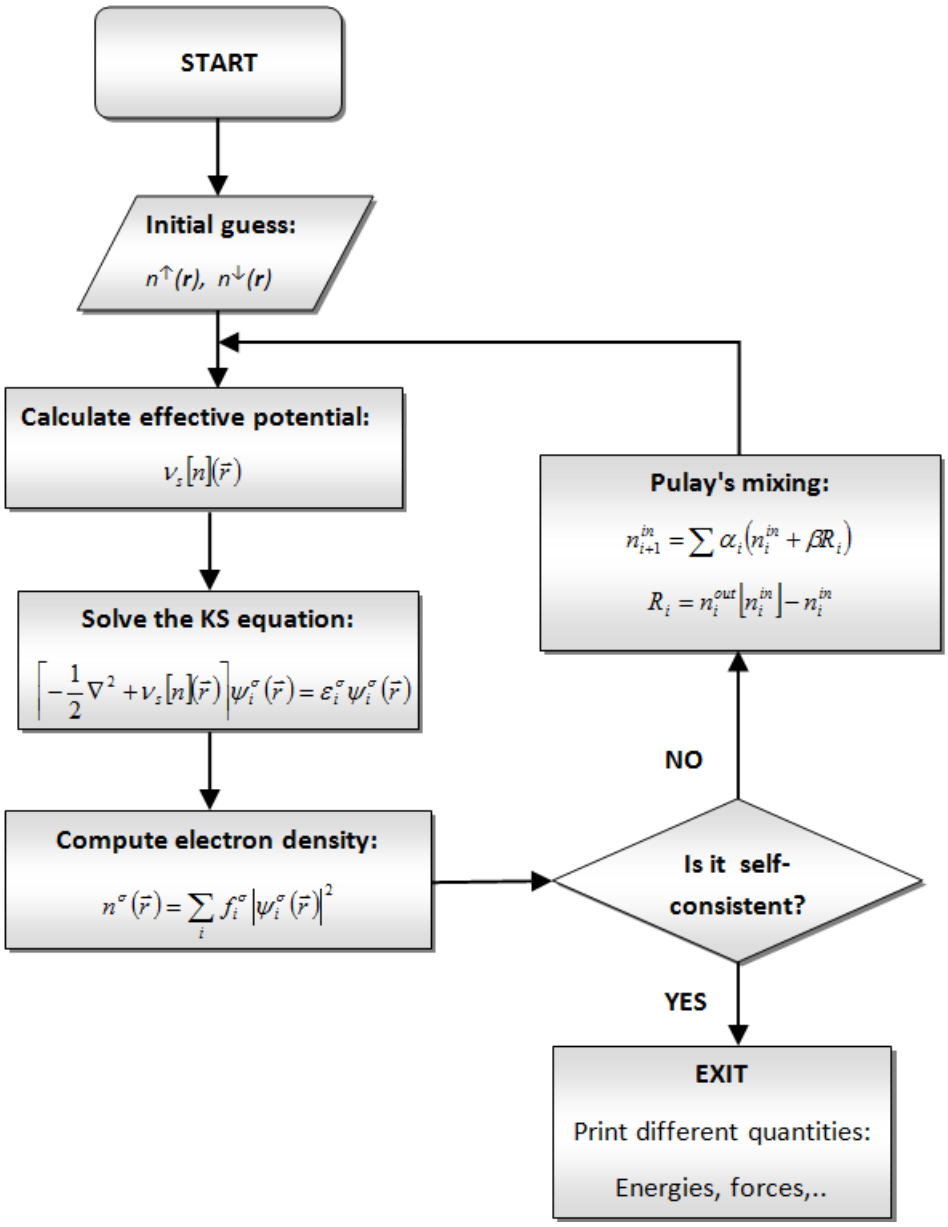

Figure 2.1: The iterative process to obtain the solution to the Kohn-Sham problem.

energy of the non-interacting electrons is (from here on, we use Hartree atomic units where $\hbar = m_e = e = (4\pi\epsilon_0)^{-1} = 1$):

$$T_s = \sum_{i=1}^{N} \langle \psi_i | -\frac{1}{2}\nabla^2 | \psi_i \rangle, \tag{2.14}$$

and the density is constructed as a sum over particle and spin indices:

$$n(\mathbf{r}) = \sum_{i,\sigma} |\psi_{i,\sigma}(\mathbf{r})|^2. \tag{2.15}$$

Now, the Hohenberg-Kohn functional appearing in the total energy expression (eq 2.13) can be written in a form:

$$F[n] = T_s[n] + U[n] + E_{XC}[n], \tag{2.16}$$

where $U[n]$ is the electrostatic Hartree term (in which the main contribution to the electron-electron interaction energy is contained), and E_{XC} is the so-called exchange-correlation functional defined as:

$$E_{XC} = (V_{ee} - U) + (T - T_s). \tag{2.17}$$

The role of E_{XC}, in more details discussed in the next subchapter, is thus to correct the inaccuracies made by the independent-particle approximation for the ground-state electron density. The resulting iteratively solved for the N electrons Schrödinger-like one-particle equation given by:

$$[-\frac{1}{2}\nabla^2 + v_{eff}(\mathbf{r})]\psi_i = \varepsilon_i \psi_i, \tag{2.18}$$

where the effective Kohn-Sham potential is:

$$v_{eff}(\mathbf{r}) = v(\mathbf{r}) + \int \frac{n(\mathbf{r}')}{|\mathbf{r} - \mathbf{r}'|} d^3r' + v_{XC}(\mathbf{r}), \tag{2.19}$$

where:

$$v_{XC} = \frac{\delta E_{XC}[n]}{\delta n(\mathbf{r})} \tag{2.20}$$

is the exchange-correlation potential. Once the ground state density n_0 is obtained, the ground state energy becomes:

$$E_0 = \sum_{i=1}^{N} \langle \psi_i | -\frac{1}{2}\nabla^2 | \psi_i \rangle + \int v_{ext}(\mathbf{r}) n_0(\mathbf{r}) d^3r + U[n_0] + E_{xc}[n_0]. \tag{2.21}$$

The iterative process to obtain the solution to the Kohn-Sham problem is presented schematically in Figure 2.1.

One has to emphasize that DFT is an *exact* theory to solve the ground state properties of an N-electron system. Practical approximations are however needed in order to represent E_{XC}. These approximations then define the accuracy for obtaining structural and energetic properties of a given system. In this thesis, the so-called generalized gradient approximation (GGA) for v_{XC} is used.

The physical interpretation of the Kohn-Sham (KS) energies ε_i (eigenvalues of Kohn-Sham orbitals) was a matter of question over many years. However the energies of the occupied KS orbitals have exact relations between ε_i and vertical ionization potentials I_i [16]:

$$\varepsilon_i \approx -I_i. \tag{2.22}$$

Moreover, the KS orbitals can sucessfully determine band structure and give information about the internal electronic structure.

2.2.3 The Exchange-Correlation Energy

The exchange-correlation energy is a concept which describes the electrostatic interaction between electron and an exchange-correlation hole. Approximations of the exchange-correlation energy, which are functionals of an electron density can be classified in the Jacob's ladder [17] with respect to the complexity of these approximations. Thus, it is important to identify which additional exact conditions are satisfied at each level of the ladder. At the lowest rung of this ladder is determined by the local density of approximation (LDA), which assume that spatial fluctuations of the density are so small that can be neglected. When the assumption is wrong, and the fluctuation can not be neglected, than the better approximation is obtain by including density

gradient, and the exchange-correlation energy is described by the generalized gradient approximation (GGA). In order to go beyond the GGA, the second (or higher) order of gradient density is included, and the functional is called the Meta-GGA[12, 17, 18]. Taking the electron density to be calculated from Eq. 2.15 an approximations for the density functional E_{xc} are: for the local density approximation:

$$E_{xc}^{LDA}[n(\vec{r})] = \int d^3n(\vec{r})[e_x(n(\vec{r})) + e_c(n(\vec{r}))]; \tag{2.23}$$

for the more general approximation, local spin density description:

$$E_{xc}^{LSDA}[n_\uparrow(\vec{r}), n_\downarrow(\vec{r})] = \int d^3n(\vec{r})[e_x(n(\vec{r}))f(\zeta) + e_c(n(\vec{r}_s), \zeta(\vec{r}))], \tag{2.24}$$

where

$$\zeta = \frac{n_\uparrow(\vec{r}) - n_\downarrow(\vec{r})}{n_\uparrow(\vec{r}) + n_\downarrow(\vec{r})} \tag{2.25}$$

is the relative spin polarization, and f(ζ) is

$$f(\zeta) = \frac{1}{2}[(1+\zeta)^{\frac{4}{3}} + (1-\zeta)^{\frac{4}{3}}]. \tag{2.26}$$

In the GGA approximation:

$$E_{xc}^{GGA}[n_\uparrow(\vec{r}), n_\downarrow(\vec{r})] = \int d^3n(\vec{r})[n_\uparrow(\vec{r}), n_\downarrow(\vec{r}), \nabla n_\uparrow(\vec{r}), \nabla n_\downarrow(\vec{r})], \tag{2.27}$$

and in the Meta-GGA, which consider the kinetic energy density as a new variable:

$$E_{xc}^{M-GGA}[n_\uparrow(\vec{r}), n_\downarrow(\vec{r})] = \int d^3n(\vec{r})e_{xc}[n_\uparrow(\vec{r}), n_\downarrow(\vec{r}), \nabla n_\uparrow(\vec{r}), \nabla n_\downarrow(\vec{r}), \tau_\uparrow(\vec{r}), \tau_\downarrow(\vec{r})], \tag{2.28}$$

where

$$\tau_\sigma(\vec{r}) = \sum_i^{occup} \frac{1}{2} \mid \nabla\psi_{i\sigma}(\vec{r}) \mid^2 . \tag{2.29}$$

Results calculated from the Kohn-Sham theory are generally improved when the approximation of the exchange-correlation energy functional of the electron density includes gradients of that electron density. Thus, the atomization energies of molecules and the binding energy of the rare-gas dimers, and lattice constants of alkali metals and transition metals are better in GGA than in LDA [19–22]. Also GGA describes correctly a bcc atom-arrangement ferromagnet of solid Fe, while it is incorrect a fcc non-magnet in LSD. More formal details on the subject are not discussed in this thesis, and the interested reader can find them in many articles and books [11, 12, 17–19, 23–26].

2.3 *Ab initio* Molecular Dynamics

One of the principal tools in the theoretical study of time-dependent behaviour of a system is molecular dynamics simulation. This computational technique provides detailed information related to conformational changes and fluctuations over the running time. One can investigate equilibrium and transport properties, the structure, dynamics and thermodynamics of many-body systems. The motions of classical objects are simulated according to Newton's laws. Generally molecular dynamics is available for both classical and quantum systems. However, the accessible time scale and also system sizes are different for these approaches.

To start, one has to consider the equation of motion for an N-particle system moving under the influence of potential $U(\boldsymbol{r}_N)$. The particles are described by their positions $(\boldsymbol{r}_1, \ldots, \boldsymbol{r}_N)$ and momenta $(\boldsymbol{p}_1, \ldots, \boldsymbol{p}_N)$. The Hamiltonian of the system is:

$$\hat{H}(\mathbf{r}, \mathbf{p}) = \sum_{I=1}^{N} \frac{\mathbf{p}^2}{2\mathbf{M}_I} + U(\mathbf{r}), \tag{2.30}$$

and the forces are derived from the potential U($\mathbf{r}$):

$$F_I(\mathbf{r}) = -\frac{\partial U(\mathbf{r})}{\partial \mathbf{r}_I}. \tag{2.31}$$

The equation of motion using the Lagrange formalism is:

$$\mathcal{L}(\mathbf{r}, \dot{\mathbf{r}}) = \sum_{I=1}^{N} \frac{1}{2} M_I \dot{\mathbf{r}}_\mathbf{I}^\mathbf{2} - \mathbf{U}(\mathbf{r}), \tag{2.32}$$

$$\frac{d}{dt}\frac{\partial \mathcal{L}}{\partial \dot{\mathbf{r}}_i} = \frac{\partial \mathcal{L}}{\partial \mathbf{r}_i}. \tag{2.33}$$

Figure 2.2 shows the algorithm for the structure optimization, for which convergence criteria is set to be maximal force between atoms in the system.

2.3.1 Born-Oppenheimer Molecular Dynamics

The Lagrangian for Born-Oppenheimer Molecular Dynamics is defined by [27–29]:

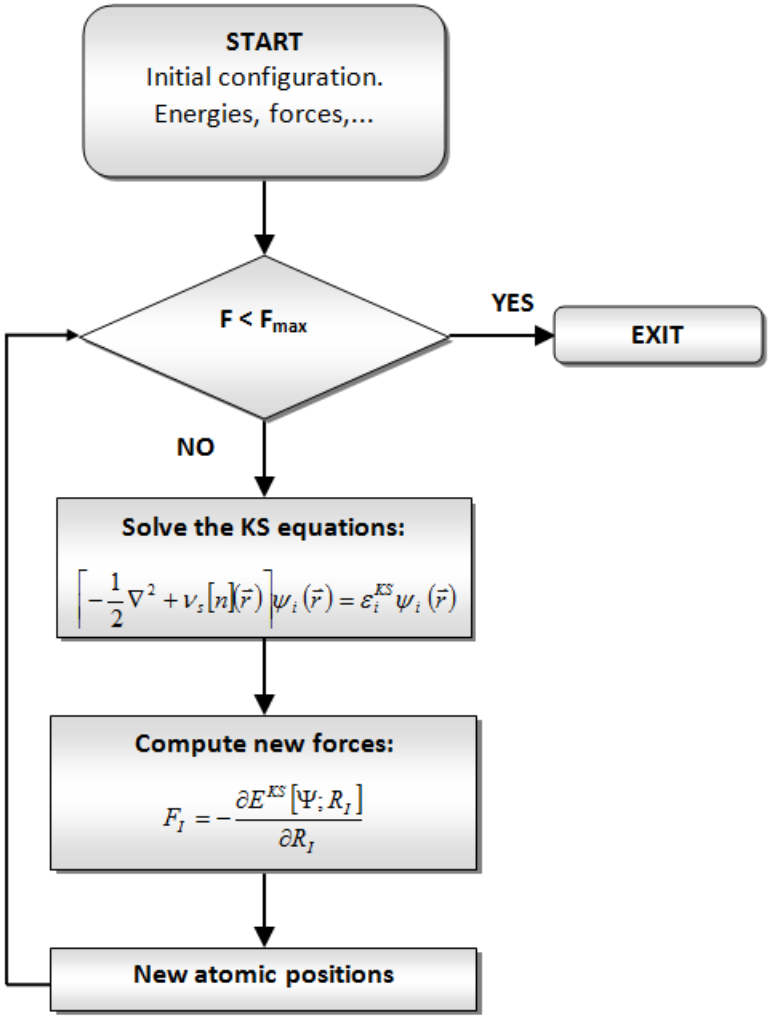

Figure 2.2: Algorithm for the structure optimization, for which convergence criteria is set to be maximal force between atoms in the system

$$\mathcal{L}_{BO}(\mathbf{r}, \dot{\mathbf{r}}) = \sum_{I=1}^{N} \frac{1}{2} M_I \dot{\mathbf{r}}_I^2 - \min_{\phi_i} E^{KS}[\phi_i; \mathbf{r}], \tag{2.34}$$

with equation of motions:

$$M_I \ddot{\mathbf{R}} = -\nabla_I [\min_{\phi_i} E^{KS}[\phi_i, \mathbf{R}]]. \tag{2.35}$$

Hence, the forces are obtained from:

$$F^{KS}(\mathbf{R_I}) = \frac{\mathbf{d}\varepsilon^{\mathbf{KS}}}{\mathbf{dR_I}} = -\frac{\partial \mathbf{E^{KS}}}{\partial \mathbf{R_I}} + \sum_{\mathbf{ij}} \mathbf{\Lambda_{ij}} (\langle \psi_\mathbf{i} | \psi_\mathbf{j} \rangle - \delta_\mathbf{ij}), \tag{2.36}$$

where the Λ_{ij} are the associated Lagrangian multipliers.

2.3.2 Car-Parrinello Molecular Dynamics

Figure 2.3 shows the scheme for Car-Parrinello Molecular Dynamics simulation. The essential idea of this technique is to provide the time-scale separation of fast electronic and slow nuclear motion by mapping the two-component quantum / classical problem onto classical / classical problem with two different energy scales. This is achieved by a suitable Lagrangian, which Car and Parrinello postulated to be [30]:

$$\mathcal{L}_{\mathrm{CP}}[\mathbf{R}^N, \dot{\mathbf{R}}^N, \{\psi_i\}, \{\dot{\psi}_i\}] = \sum_I \frac{1}{2} M_I \dot{\mathbf{R}}_I^2 + \sum_i \frac{1}{2} \mu \langle \dot{\psi}_i | \dot{\psi}_i \rangle - E\left[\{\psi_i\}, \mathbf{R}^N, \{\alpha_v\}\right] + \sum_v \frac{1}{2} \mu_v \dot{\alpha}_v^2, \tag{2.37}$$

where the first term is the kinetic energy of the nuclei, the second term is the fictitious kinetic energy of electrons (μ is a fictitious mass to define the proper time scale), the third term is the electronic energy and the last term deals with a set of constraints. The ψ_i's are subject to orthogonality constraints:

$$\int_\Omega d^3 r \psi_i^* \psi_j = \delta_{ij}. \tag{2.38}$$

The Car-Parrinello equations of motion are defined to be of form:

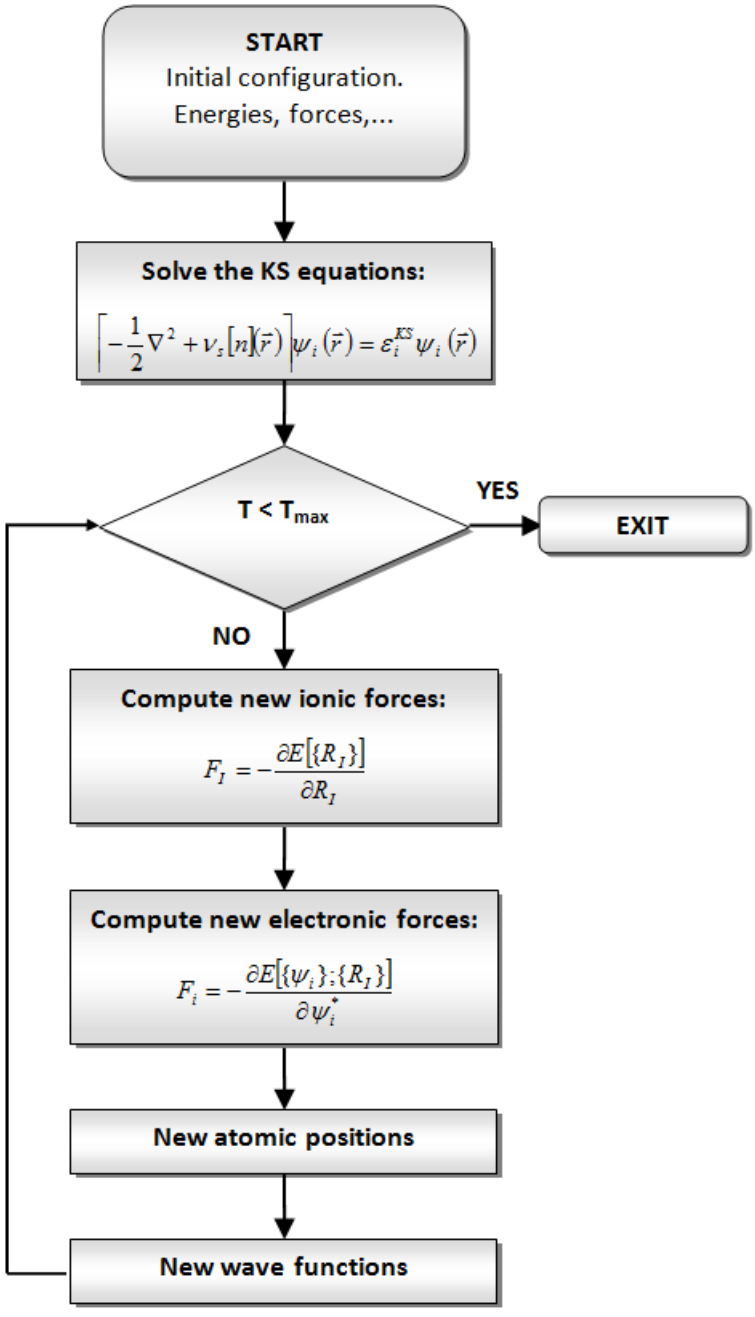

Figure 2.3: Algorithm for the Car-Parrinello Molecular Dynamics. Simulation is ended when maximal time of running is reached.

$$\mu\ddot{\psi}_i(\mathbf{r},t) = -\frac{\delta E}{\delta\psi_i^*(\mathbf{r},t)} + \sum_k \Lambda_{ik}\psi_k(\mathbf{r},t), \tag{2.39}$$

$$M_I\ddot{R}_I = -\nabla_{R_I}E, \tag{2.40}$$

$$\mu_v\ddot{\alpha}_v = -\frac{\delta E}{\delta\alpha_v}, \tag{2.41}$$

where Λ_{ik} are Lagrange multipliers needed to satisfy the constraints 2.31.

2.4 Pseudopotentials

It is known that only valence electrons contribute to bonding between atoms in molecules and in solid state. The principal idea of a "pseudopotential" is to replace the strong Coulomb potential between valence electrons and the nucleus by a soft one. The constructed pseudopotential is a weaker potential which replaces the true potential inside a pre-defined core. This effective potential is constructed from the nuclear potential screened by the core electrons, in a way that outside of the defined core region the total potential and the pseudopotential have the same behaviour. This approach diminishes the number of basis functions for expression of the valence states. The constructed pseudopotentials are calculated and tabulated once for each atom, and are transferable to different chemical environments. All relativistic effects can be described in the constructed pseudopotentials. The smoother pseudo wave functions for the valence electrons result in a significant reduction of the computational effort in solving for the Kohn-Sham problem.

Most modern pseudopotential calculations are based upon *ab initio normconserving* potentials, such as Troullier-Martins pseudopotentials [31] which are accurate and transferable, meaning that describes valence properties in different environments including atoms, ions, molecules, and condensed matter. Other kind of pseudopotentials, so-called *ultrasoft pseudopotentials* express pseudofunctions as a sum of a smooth part and a more rapid varying function localized around each ion core [32, 33].

In this thesis norm-conserving Troullier-Martins pseudopotentials were chosen to conduct molecular dynamic simulations, and there are specific rules, which are required when one wants to generate the pseudopotentials. According to Hamann, Schluter, and Chiang [34] certain norm-conserving conditions have to be accomplished, such as: all-electron and pseudo valence eigenvalues agree for the chosen atomic reference configuration and beyond a chosen radius (cutoff radius), the logarithmic derivatives of the all-electron and pseudo wavefunctions have to agree at cutoff radius, and the integrated charge for each wavefunction agrees inside the core agrees, and the last, the first energy derivative of the logarithmic derivatives of the all-electron and pseudo wavefunctions agrees outside the core [35].

2.5 The Projector Augmented Wave Technique

Another way to solve Kohn-Sham equation is to use Projector-Augmented plane-Wave (PAW) method by Blöchl in 1994 [33]. In 2005, an implementation of this method to real space grids (GPAW) was presented [36]. In this approach the all-electron Kohn-Sham wavefunction is transformed into auxiliary wave functions. Auxiliary wave functions are smooth everywhere, while the all-electron wave functions contain rapid oscillations. Both core and valence states are described inside the augmentation region on atom centred radial grid, while the valence states are represented on real space grid in the interstitial region. The atomic augmentation sphere is determined by a radial cutoff. The radial cutoff has a similar meaning as the cutoff radius for a pseudopotential.

Since "all chemistry" happens in the valence region, the core states are frozen, and only valence states are self-consistently solved. Figure 2.4 shows an example of the generated partial waves for gold atom. Fig. 2.4A shows all of the all-electron partial waves and Fig. 2.4B shows the valence states ($5d$ $6sp$ states). Localized inside the augmentation sphere, smooth projector functions act on the partial waves and the linear transformation given by atom-centred all-electron wave function $\phi_a(\mathbf{r})$, the corresponding smooth partial waves $\tilde{\phi}_a(\mathbf{r})$, and projector functions $\tilde{p}_i^a(\mathbf{r})$, define alteration between "smooth" (or "pseudo") wavefunctions $|\tilde{\psi}\rangle$ and the "all-electron" wavefunctions $|\psi\rangle$:

$$|\psi_n\rangle = \hat{\mathcal{T}}|\tilde{\psi}_n\rangle, \tag{2.42}$$

$$\tilde{\mathcal{T}} = 1 + \sum_a \sum_i (|\phi_i^a\rangle - |\tilde{\phi}_i^a\rangle)\langle\tilde{p}_i^a|, \tag{2.43}$$

where n is a band index denoted principal quantum number, $\hat{\mathcal{T}}$ linear transformation. Summarizing, the all-electron and pseudo wavefunctions have different shapes in the core and the valence region, but they match exactly in the valence region. The quantities like true all-electron density is obtained from the wavefunctions, the atom-centered smooth-core electron density and the correction, which arise from the difference between atom-centered all-electron and pseudoelectron densities:

$$n(\mathbf{r}) = \tilde{n}(\mathbf{r}) + \sum_a (n^a(|\mathbf{r} - \mathbf{R}^a|) - \tilde{n}^a(|\mathbf{r} - \mathbf{R}^a|)), \tag{2.44}$$

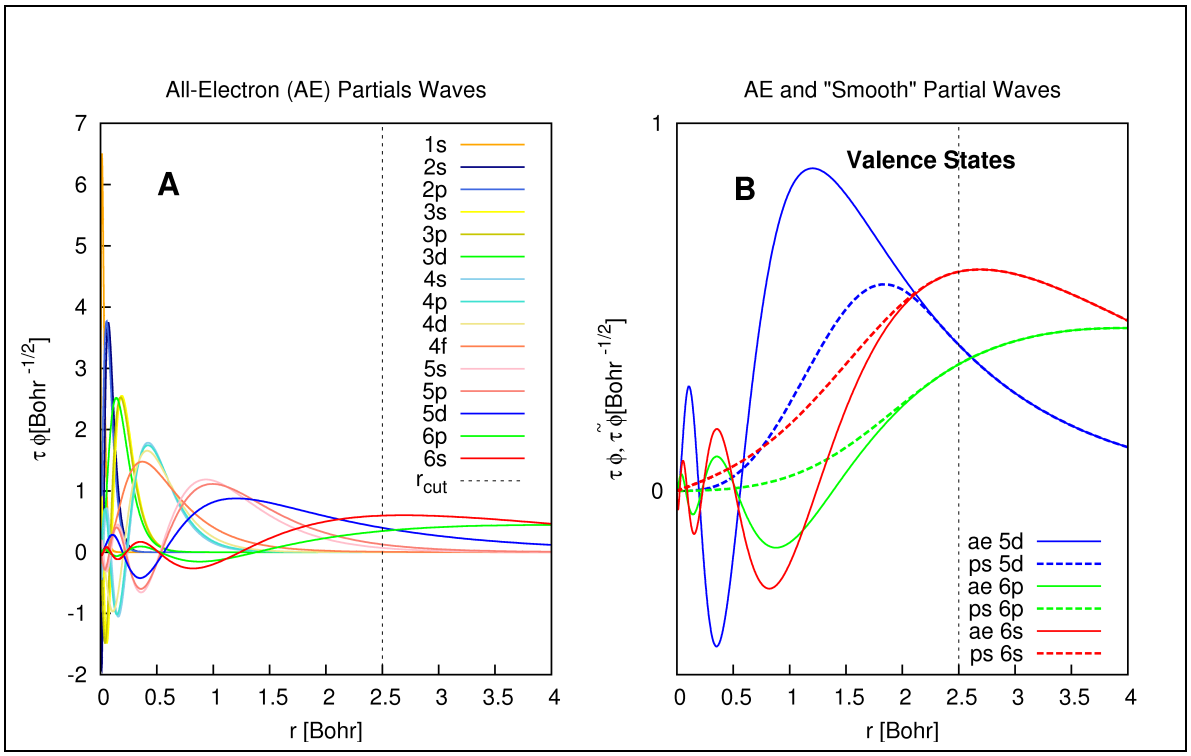

Figure 2.4: All-electron wavefunctions and pseudo-wavefunctions generated for gold atom in its ground state, obtained with Density Functional Theory at an GGA (PBE) level. The figure displays: A - all-electron partial waves; B: transformed all-electron and auxiliary partial waves for valence states; r_{cut} is the radial cutoff which define augmentation sphere.

where:

$$\tilde{n}(\mathbf{r}) = \sum_{n}^{val} f_n |\tilde{\psi}_n(\mathbf{r})|^2 + \sum_a \tilde{n}_c^a(|\mathbf{r} - \mathbf{R}^a|) \tag{2.45}$$

is the pseudoelectron density,

$$n^a(\mathbf{r}) = \sum_{i_1 i_2} D^a_{i_1 i_2} \phi^a_{i_1}(\mathbf{r}) \phi^a_{i_2}(\mathbf{r}) + n^a_c(\mathbf{r}) \tag{2.46}$$

is atom-centered all-electron density, and

$$\tilde{n}^a(\mathbf{r}) = \sum_{i_1 i_2} D^a_{i_1 i_2} \tilde{\phi}^a_{i_1}(\mathbf{r}) \tilde{\phi}^a_{i_2}(\mathbf{r}) + \tilde{n}^a_c(\mathbf{r}) \tag{2.47}$$

is atom-centered pseudodensity.

The total PAW energy is given by:

$$E = \tilde{E} + \sum_a (E^a - \tilde{E}^a). \tag{2.48}$$

First term is so-called the soft energy contribution evaluated on three dimensional grid in real space, while the second and third term are calculated inside the core region on radial grid. This scheme allows to obtain a correct value for energy calculated on two incompatible grids. The total energy is also expressed by the auxiliary and the smooth wavefunctions.

2.6 The Nudged Elastic Band Technique

One of the interesting subjects in theoretical chemistry and physics is finding the most optimal reaction path required for transformation of reactants to products. Such a path is assigned to so-called *minimum energy path* (MEP) or *minimum energy reaction path* (MERP) and describes rearranging atoms or molecules from one stable configuration to another [37–39]. Such reaction path is associated with conformational changes or with electronic states changes. The local minima are connected through a saddle point (transition state). The saddle point denotes the potential energy maximum along the MEP related to the activation energy barrier. Finding an accurate energy profile, which is the potential energy along the path is not a straightforward task due to a large relaxation of the substrate. One class of method to analyse transitions in classical systems is a *chain-of-states methods*, in which chain of connected images of the system is created. Generated images are located along a line between the stable configurations. All images, after simultaneously optimized, should lie near the MEP. The images are defined as:

$$S^{PEB}(\mathbf{R}_i, \ldots, \mathbf{R}_{P-1}) = \sum_{i=0}^{P} V(\mathbf{R}_i) + \sum_{i=1}^{P} \frac{Pk}{2}(\mathbf{R}_i - \mathbf{R}_{i-1})^2, \tag{2.49}$$

where P+1 is a number of images, $\mathbf{R}_0$, $\mathbf{R}_P$ are the positions of the initial and the final images, which are fixed over the whole simulation. PEB refers to the *plain elastic band*. The equation [2.42] requires a modification in order to provide the correct MEP. One of the important issues in the MEP finding is a good initial guess for images. Choi and Elder [40] proposed the Local Update Planes (LUP), where the chain of images is accomplished by local tangent estimated with respect to the path defined by the previous and later image in the chain:

$$\hat{q}_i = \frac{\mathbf{R}_{i+1} - \mathbf{R}_{i-1}}{|\mathbf{R}_{i+1} - \mathbf{R}_{i-1}|}, \tag{2.50}$$

and then relaxing the image according to:

$$\frac{\partial \mathbf{R}_i}{\partial t} = -\nabla V(\mathbf{R}_i)[1 - \hat{q}_i \hat{q}_i]. \tag{2.51}$$

In this thesis the reaction path for catalysis presented in section 3.3.2 was obtained by using the approach, which combines the plain elastic band method with the local update plane and is denoted by the nudged elastic band method (NEB) [41–43]. Thus,

the images are connected through spring forces while concerning unit tangent to the path. This technique eliminates the so-called "corner-cutting" which overestimates the saddle point energy and decouples the dynamics (the relaxation) from the discrete representation of the path. Therefore, the force on each image placed between fixed images in the NEB method is constructed from:

$$\mathbf{F}_i^0 = -\nabla V(\mathbf{R}_i)|_\perp + \mathbf{F}_i^s \cdot \hat{\tau}_\parallel \hat{\tau}_\parallel, \tag{2.52}$$

and later from:

$$\mathbf{F}_o^{NEB} = \mathbf{F}_i^0 + f(\phi_i)(\mathbf{F}_i^s - \mathbf{F}_i^s \cdot \hat{\tau}_\parallel \hat{\tau}_\parallel), \tag{2.53}$$

where $\hat{\tau}_\parallel$ is the unit tangent to the path and $\nabla V(\mathbf{R}_i)|_\perp$ refer to projection of the perpendicular component of ∇V and the parallel component of the spring force, ϕ_i denotes a switching function for so-called "kinky" paths. Although the NEB method is an effective technique, the energy of transition state (saddle point) is obtained by interpolation, and this leads to wrong quantities. The issue was elucidated in the climbing image NEB (CI-NEB) [44], where the force acted on the image ($\mathrm{i_{max}}$) with the highest energy is given by:

$$F_{i_{max}} = -\nabla E(\mathbf{R}_{i_{max}}) + 2\nabla E(\mathbf{R}_{i_{max}})|_\parallel = -\nabla E(\mathbf{R}_{i_{max}}) + 2\nabla E(\mathbf{R}_{i_{max}}) \cdot \hat{\tau}_{i_{max}} \hat{\tau}_{i_{max}}. \tag{2.54}$$

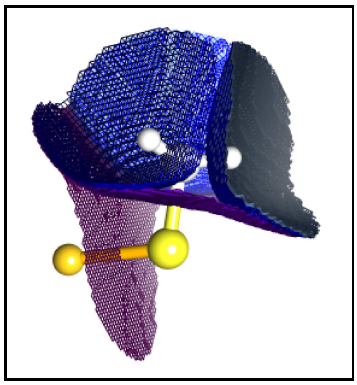

Figure 2.5: The charge-dividing surfaces according to the Bader analysis for gold-methylthiolate molecule $AuSCH_3$.

2.7 The Methods of Analysis

2.7.1 The Bader Charge Analysis

Many chemical properties of materials are analysed in terms of charge transfer between atoms. However, atom charges are not defined by quantum mechanical theory. Thus, it is an ambiguous issue to describe how electrons are shared among atoms in chemical compounds, and one should note, that there are several methods to decompose charge into atoms [45]. None of them is exact, and the obtained effective charge may show considerable variations between different schemes. Mainly because they are focused on an estimation of a delimit between two atoms. Examples of such methods are Mulliken population analysis, Voronoi Deformation Density and Bader charge analysis. The first method analyses the population of wavefunctions, and the Voronoi Deformation Density defines regions which are assigned to a nearest-neighbour atom. In this thesis, the Bader analysis was chosen, since it works well in systems that have both heavy and light elements. This method separates atoms from each other in places, where the charge density reaches a minimum between atoms [46]. It introduces *bond critical points* (bcp) which divides the space into *Bader regions*, whose boundaries are constructed from the zero-flux surfaces, and they intersect these points, as it is shown in figure 2.5. The separation of a space is given by:

$$\nabla\rho(\mathbf{r}) \cdot n(\mathbf{r}_s) = 0, \tag{2.55}$$

for every point r_s on the surface, where $n(\mathbf{r}_s)$ is the unit normal vector on the surface defined by the radius r_s

2.7.2 Projected and Local Density of States

The total density of states is defined by:

$$\rho(\varepsilon) = \sum_n \langle\psi_n|\psi_n\rangle\delta(\varepsilon - \varepsilon_n), \tag{2.56}$$

where ψ_n is the Kohn-Sham eigenstate with the corresponding eigenvalue ε_n. Since materials are often not homogeneous, they contain different types of atoms, or they are disordered by impurities, then it is very useful to obtain information associated with a particular atom. For this purpose, the analysis of *local density of states* is introduced.

The local density of states is calculated as the square modulus of the all-electron wave-function overlaps and multiplied by normalized gaussians of a certain width, and is written as:

$$\rho_i(\varepsilon) = \sum_n \langle\psi_n|i\rangle\langle i|\psi_n\rangle\delta(\varepsilon - \varepsilon_n), \tag{2.57}$$

where $1 = \sum_i |i\rangle\langle i|$ and $\{|i\rangle\}$ is a local atomic basis.

The Kohn-Sham states are also analyzed with respect to the globular angular momentum (called *PDOS*). Taking the center of the expansion to be the center of mass of the cluster, one calculates the coefficients:

$$c_{i,\ell}(R_0) = \sum_m \int_0^{R_0} r^2 |\phi_{i,\ell m}(r)|^2 dr, \tag{2.58}$$

where

$$\phi_{i,\ell m}(r) = \int Y^*_{\ell m}(\hat{r})\psi_i(\mathbf{r})d\hat{r}, \tag{2.59}$$

and i is the index of the Kohn-Sham state ψ, $Y_{\ell m}$ is the spherical harmonic function with ℓ as the angular quantum number and m as the magnetic quantum number. Angular momenta up to $\ell = 6$ have been considered. The expansion is made in a sphere of radius R_0, which (in this thesis) encompasses the metal core of monolayer protected clusters.

3 Results

This thesis focuses on the results discussed in the articles [I-VI] which present the density functional studies of the electronic, structural and chemical properties of a metal-thiolate polymers and doped ligand-protected gold clusters, and the catalytic properties of small bare and partially ligand-protected gold clusters.

The first section describes theoretical characterization of cyclic thiolated copper, silver and gold clusters. The second section investigates modifications of a structurally known ligand-protected gold cluster, by introducing impurities, either in the well-defined cluster core, or in the protecting ligand shell. Later, a possible application for the thiolated cluster as a building block is investigated. In the last section catalytic properties of small bare and partially protected clusters are discussed.

3.1 Noble Metal Thiolate Polymers

In this section electronic structure calculations of cyclic motifs $(MeSCu)_x$, $(MeSAg)_x$, and $(MeSAu)_x$ for x=1-12 are discussed. In addition, catenane and helix-like configurations were studied. The low energy isomers are presented only for Cu and Ag, as the gold systems have been reported elsewhere [9]. Selected ring, catenane and helix structures are reported in Figure 3.1.

Several ring isomers for a given x were relaxed to a local minimum and the ones with the lowest energy are shown in Figure 1 of Article VI, and partially reproduced in figure 3.1. Results show that in all cases the methyl thiolates are bonded in bridge configurations, building up closed rings or crowns. The metal-thiolate oligomers ($x \leq 4$) are planar, whereas the larger polymers develop a zigzag motif. This structural motif develops and becomes clearer for the larger sizes. For all odd systems, the structure has to incorporate a "structural defect", whereas the even number complexes have all metal atoms in a plane. The metal-thiolate dimer is the only system for which methyl groups prefer torsional orientation in cis- over the trans-configuration. Table 2 in Article VI lists values which reveal rapid convergence of certain structural parameters, such as the metal-sulfur bond length and the sulfur-metal-sulfur angle for all coinage metals and the metal-sulfur-metal angle for Au and Ag.

Table 3.1 reports the stability of low energy isomers $(MeSM)_x$ (M = metal, x = 1-12),

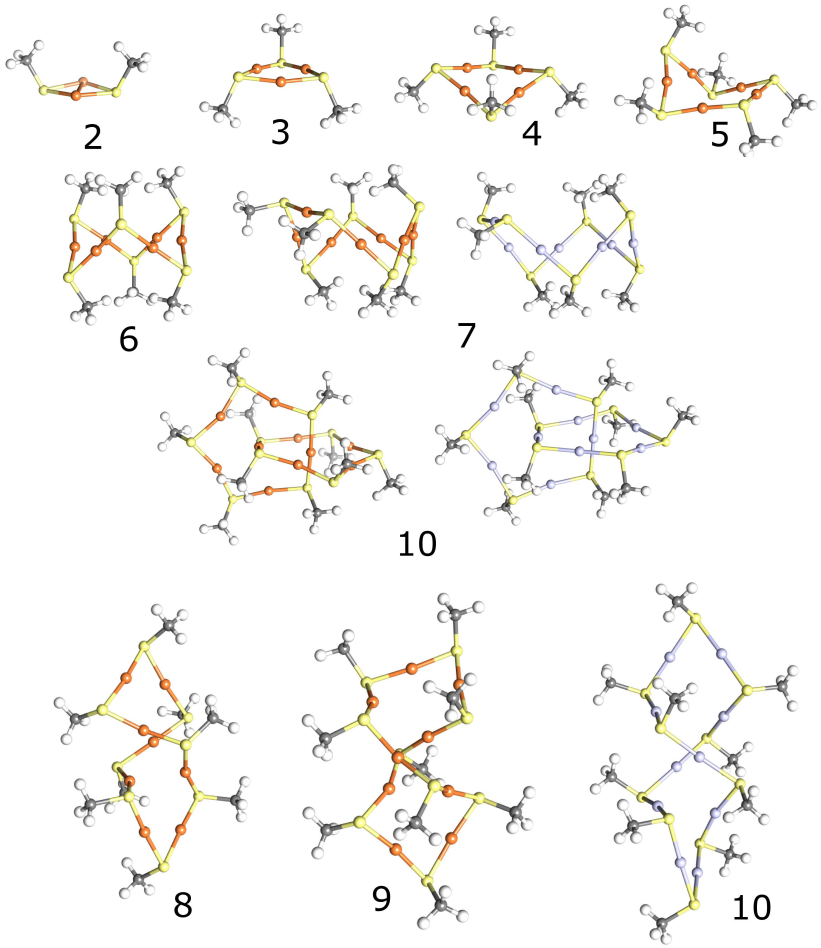

Figure 3.1: Low energy isomers of ring structures for $(MeSM)_x$ with x=2-7, and below, two catenane and three helix-like optimized structures. Atomic color codes: Brown (Cu), gray(Ag), yellow (S), black (C) and white (H).

which are calculated from the fragmentation energies (E_f) according to:

$$E_f = (x \cdot E[MeSM] - E[(MeSM)_x])/x \tag{3.1}$$

Table 3.1: The fragmentation energy to MeSM units per unit in eV.

	Cu	Ag	Au
$(MeSM)_2$	1.18	0.87	0.56
$(MeSM)_3$	2.05	1.62	1.76
$(MeSM)_4$	2.15	1.73	1.99
$(MeSM)_5$	2.12	1.72	2.00
$(MeSM)_6$	2.13	1.73	2.01
$(MeSM)_7$	2.13	1.73	2.00
$(MeSM)_8$	2.16	1.73	2.01
$(MeSM)_9$	2.15	1.72	2.00
$(MeSM)_{10}$	2.15	1.73	2.01
$(MeSM)_{11}$	2.13	1.72	2.00
$(MeSM)_{12}$	2.15	1.72	2.00

and they also indicate a fast converge, with higher stability for the even cluster then the odd. This is related to the possibility of even sized clusters to adopt a more regular zigzag pattern. Other parameters which are clearly related to the stability of these rings are the bond strength between MeSM and M-M cohesion. The bond length in the monomer for each coinage metal is in fair agreement with the metal-sulfur bonds in the rings. Moreover, the metal-sulfur bond is stronger than the metal-metal bond for all considered systems, which explains the bridge configurations of the methyl thiolates.

In addition to the structures based on a mono-cyclic motif, catenane and helix structures were investigated. Catenane structures with two cyclic rings that inter-penetrate each other have been experimentally observed [47, 48]. In Ref. [47] $(AuSC_6H_4 - p - CMe_3)_{10}$ and $(AuSC_6H_4 - o - CMe_3)_{12}$ were prepared and structurally characterized, whereas in Ref. [48] the formation of catenanes with chiral properties for the undecamer with RS=[2,3,4,6-tetra-O-acetyl-β-1-D-thioglucopyranosato-S] containing $[Au_5S_5]$ and $[Au_6S_6]$ interlocking rings were studied. It was found that the two pentamers and/or hexamers inter-penetrate with one Au atom of one ring situated close to the center of the other ring. In addition, helix structures are known to be relevant for gold thiomalate [49], which is used as an anti-arthritic drug [50].

Here, catenane structures were theoretically investigated for $(MeSM)_x$ with x=8-12, and M=Cu, Ag, Au. Exploration reveals that the smallest stable catenane is $(MeSM)_{10}$

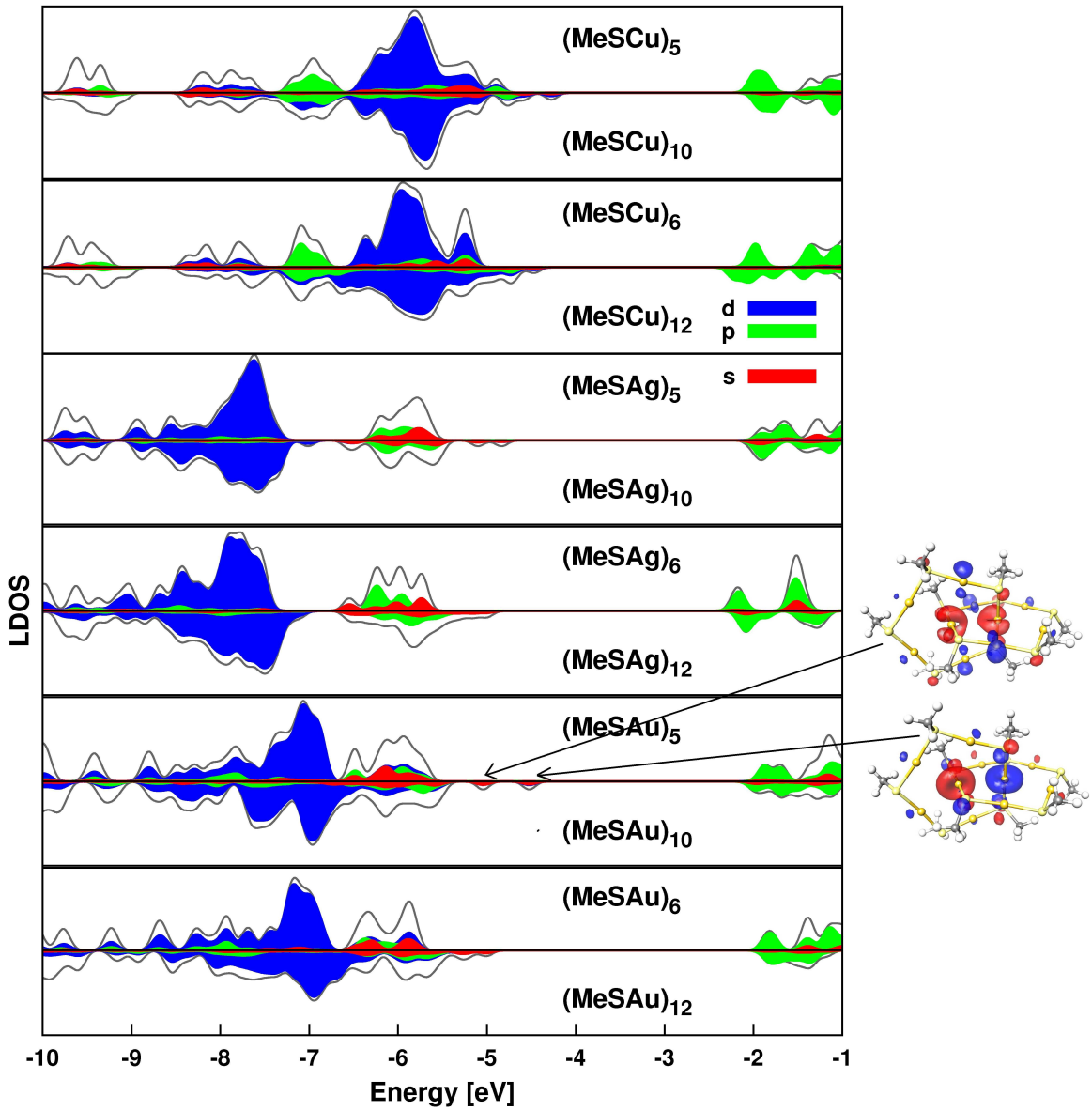

Figure 3.2: Electronic density of states (EDOS) for cyclic $(MeSM)_5$, $(MeSM)_6$ and catenane conformation $(MeSM)_{10}$ and $(MeSM)_{12}$. The total density of state is marked by a grey line. The shaded areas correspond to the local density of stated associated with metal atoms. Blue, green and red color denote d, p, and s contribution, respectively. The one-electron Kohn-Sham energies have been broadened with a 0.1 eV Gaussian. The DOS has been normalized by devision of the number of (MeSM) units in each cluster. The Kohn-Sham orbitals for HOMO and HOMO-1 are shown for $(MeSAu)_{10}$.

and complexes with $x < 10$ were highly unpreferable with respect to the corresponding ring structure. All studied catenane structures have two (for deca- and dodecamer) or three (for undecamer) metal-sulfur distances: one longer distance, that involves a metal at the center of the ring, and the others are shorter. The decamer has two close-to-planar pentamer interlocking rings, where the ring-ring interaction counteracts some of the bent structure present for the single pentamer geometry. The undecamer is interesting, since two rings: penta- (originally almost planar) and hexamer (zigzag) are interacting. Again, the steric interaction between the rings counteracts the zigzag structure and the rings turns more planar than in the mono-cyclic case. Moreover, a combination of odd and even number of interlocked rings develops structural defects, and the distances between metal atoms in the periphery of the pentamer and the center atom of the pentamer are more regular, in contrary to the hexamer, in which the distances between the atoms vary substantially. The undecamer posseses three metal-sulfur bond lengths defined by the localization of metal atoms: in the center of the pentamer, in the center of the hexamer, and in the periphery of the rings. The last studied catenane is the dodecamer with two hexamer crown-like rings where the metal atoms are arranged on two planes. Metal atoms lying along transverse diameter of the whole compound define the intersection of these planes. The angle between these planes is determined by three metal-metal atoms, which are sitting on the periphery of the subunits.

Helix structures are experimentally known to be relevant for gold thiolate complexes [49], and it was recently proposed that helical structures for $(MeSAu)_x$ with x=6-9 [51] are favoured over the mono-cyclic rings. For this study, several selected sizes were investigated. As a starting guess for structural optimization various models were built and checked including those reported in Ref. [51]. Contrary to the finding of Shao *et al.* [51] the results reveal that the helix-like structure is not energetically preferred. However, in the studied size range, helix-like complex for $(MeSAg)_8$ and $(MeSCu)_8$ have been found as the only ones to be energetically favourable over the other structures.

The electronic density of states (EDOS) for the low energy homoleptic polymers are reported in Figure 4 of Article VI, and Figure 3.2 reports EDOS for catenane structures together with the corresponding mono-cyclic rings. Both figures reveal that these systems are "molecular" in the sense that all the considered sizes of mono-cyclic rings and catenanes have a large HOMO-LUMO (HL) gap, although it issignificantly reduced for the catenanes. The smallest gap are found for the dimer: 2.06 eV, 2.13 eV, and 1.50 eV for M= Cu, Ag, and Au, respectively. On the other side, the largest HL gaps for Ag and Au are calculated for the tetramers; 3.82 eV and 3.97 eV for Ag and Au, respectively. For Cu, the largest HL separation is found for the hexamer (3.17 eV). The shaded part of the spectra in Figure 3.2 is the density of states projected locally onto the metal atoms (LDOS). States close to the HOMO level of the mono-cyclic rings are of s-character, Cu and Au also show some weights on d. In all cases, these

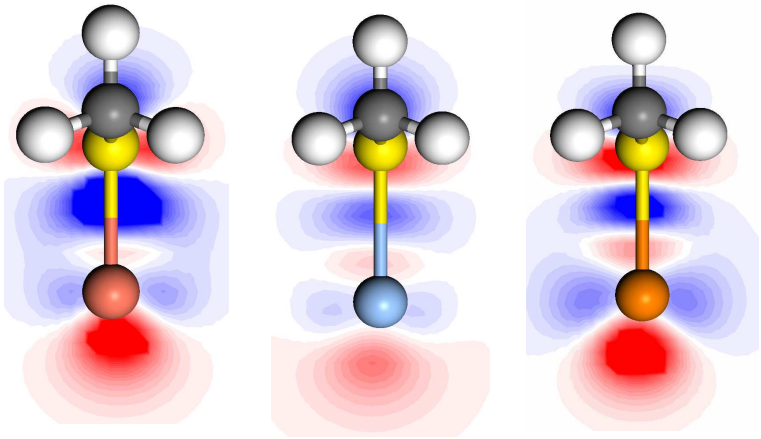

Figure 3.3: Slices through the charge density differences for MeSCu, MeSAg and MeSAu. Blue corresponds to charge gain and red to charge depletion. Iso-surfaces are shown in the range [-0.1,0.1] (e/Å^3).

states are hybridized with sulfur *p*-states. The HOMO and HOMO-1 of the interlocked rings (catenanes) are anti-bonding and bonding combinations of *s*-derived Au states.

The bond character of different metal-thiolate complexes is determined by the Bader analysis and the charge density difference analysis. The first shows that the largest charge separation is obtained for copper, whereas the smallest is calculated for gold. Figure 3.3 shows the rearrangement of the charge for MeSCu, MeSAg, and MeSAu calculated as:

$$\Delta\rho = \rho(\mathrm{MeSM}) - \rho(\mathrm{M}) - \rho(\mathrm{MeS}). \tag{3.2}$$

This analysis displays clear difference between bond types of these complexes. In the case of MeSCu, charge is depleted from the metal site and polarized towards the thiolate, whereas MeSAu pronounce a clearer sign of a covalent bond type with both charge depletion and accumulation along the Au-S bond. In MeSAg charge rearrangement is less pronounced which is consistent with a longer bond distance and weaker bond strength.

3.2 Thiolate Protected Gold $Au_{25}(SR)_{18}^{-}$

$Au_{25}(SR)_{18}^{-}$ is an example of a small nanoparticle with a distinct molecule-like HOMO-LUMO energy gap (ca. 1.33 eV), as measured by voltammetry and spectroscopy. It can be synthesized in respectable yields with high monodispersity [4, 5, 52, 53], is stable in air and at room temperature, and the ligands can be readily replaced by ligand exchange reactions. Theoretical studies based on DFT have shed light onto the electronic structure of the structurally determined compounds [54–56], and in fact, in the case of the $Au_{25}(SR)_{18}^{-1}$ cluster, correctly predicted the observed atomic geometry [55]. The electronic shell closing in the metal core, based on a simple counting of the valence electrons, was observed to explain the stability of several all-thiolate, thiolate-phosphine and phosphine-halide protected gold clusters [54]. If one writes the composition of a protected cluster as $L_m Au_N X_y^z$ where z is the charge, L is a "weak ligand" (e.g. phosphine, m=0 in case of all-thiolate-protected compounds) and X is an electron-withdrawing ligand (which already may contain Au atoms), the stable clusters obey the rule:

$$N - y - z = n^*; \tag{3.3}$$

where $n^* = 2, 8, 34, 58, \ldots$ corresponds to the electron shell-closing numbers for metal clusters, and N is the number of valence electrons of the core metal atoms. Thus, the $Au_{25}(S(CH_2)_2Ph)_{18}^{-}$ cluster has a shell closing at 8 electrons:

$$n^* = 8 = 13 - 6 - (-1). \tag{3.4}$$

The theoretical model of the methylthiolate-passivated $Au_{25}(SR)_{18}^{-1}$ cluster anion can be written as $Au_{13}[Au_2(SCH_3)_3]_6^{-1}$ and is coined to the "divide-and-protect" structural motif [57]. The motif is characterized by the presence of two kinds of gold atoms: core atoms, formally in a metallic Au^0 state, and gold atoms in the ligand shell, formally oxidised Au^I. The latter play a role for protecting the core. The electronic density of states (EDOS) of the cluster [58] near the HOMO-LUMO gap reveals a 3-fold degenerate HOMO level, whereas LUMO is 2-fold degenerate. The character of the electronic states was shown to be mainly of P-character for the HOMO state, whereas the LUMO has D-symmetry. This can be understood within a model for delocalized core Au(6s) electrons in a spherical background potential [59] with an electronic shell structure of $1S^21P^6$ for the occupied superatom states and D^{10} for the lowest unoccupied superatom states. The anionic core of the cluster contains 14 valence electrons, in which 6 from 14 form strong polar covalent bonds with the protecting ligands.

Therefore, each semi-ring can be regarded as $[(MeS)_3Au_2]^-$ bound to an (effectively) icosahedral Au_{13}^{5+} core. These electronically stable and chemically protected Au compounds of Eq. 3.4 were coined as "superatom complexes". The behaviour of such complexes requires understanding of the impact of impurities on their properties, which may help to identify particular phenomena affected by specific material parameters. As an example, bimetal nanoparticles consisting of gold and one of the platinum-group metals are known to improve the selectivity of low-temperature oxidation reactions. The catalytic properties of a given cluster may be drastically affected by changing the atom or electron count just by one, and it is therefore of great interest to study how mixing palladium into ultra-small gold clusters would change their atomic structure and electronic properties. Thus, the structural, electronic, optical and capacitive charging properties of $PdAu_{24}(SMe)_{18}^{z}$ complexes, with various charges states between -3 and +3 were investigated [Article II]. Additionally, series of exchanges of the original $-SCH_3$ ligands of $Au_{25}(SR)_{18}^{-}$ with the thiolates of more electron-withdrawing $-SCH_2Cl$ ligands were examined to elucidate how the charge distribution in the nanoparticle changes over the course of the ligand exchange reaction [Article IV]. In the end of this section, dimeric clusters of superatoms will be discussed.

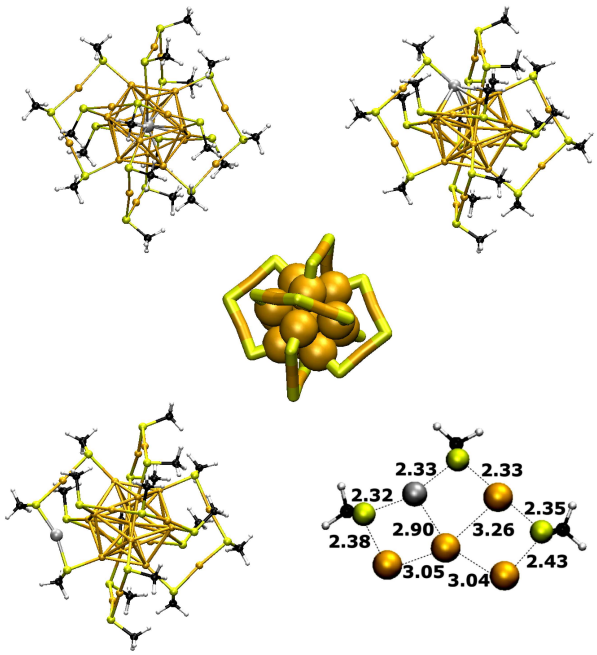

Figure 3.4: The structures of the $PdAu_{24}(SR)_{18}^{-2}$ clusters. Top left and right: C and S isomers, respectively. Bottom left: L isomer. Bottom right: blow-up of the RS-Pd-SR-Au-SR ligand and the closest core surface atoms in the L isomer. Note the slight relaxation of the Pd atom towards the core Au atom(s). Center: the general "divide and protect" structure motif of $Au_{25}(SR)_{18} = Au_{13}[Au_2(SR)_3]_6$ highlighting the near-icosahedral Au_{13} core. Au: orange, Pd: gray, S: yellow, C: black, H: white

3.2.1 Doping the $Au_{25}(SR)_{18}^{-}$ Cluster by Palladium

This study was motivated by the experiments conducted in R.W. Murray's group [60] which, for the first time, synthesized bimetal and mixed-ligand $M_xAu_{25-x}(SR)_y(SR')_{18-y}$ (M = Pd, Pt) clusters and characterized their composition, electrochemistry and optical properties. It was confirmed by mass spectrometry that the count of thiolates was always 18 and that the metal composition for Pd was $PdAu_{24}$, i.e., only mono-doping was observed for this size. In order to fulfil the requirement in Eq. (3.4), the $PdAu_{24}(SR)_{18}^{z}$ cluster has to be double anionic (z = -2). The cluster has three possible sites for doping: the center of the nearly-icosahedral Au_{13} core (C isomer), one of the 12 Au sites on the surface of the core (S isomer) or the Au site in one of the six equivalent $Au_2(SR)_3$ ligands (L isomer) (Figure 3.4). The changes in the structural parameters are minor, and a comparison between the isomers reveals that the most stable is the C isomer, followed by the S and L isomers.

Analysis of the frontier orbitals (HOMO and LUMO states) using PDOS, shown in Figure 3.5 indicates that, in comparison to undoped $Au_{25}(SR)_{18}^{-1}$, C isomer has a

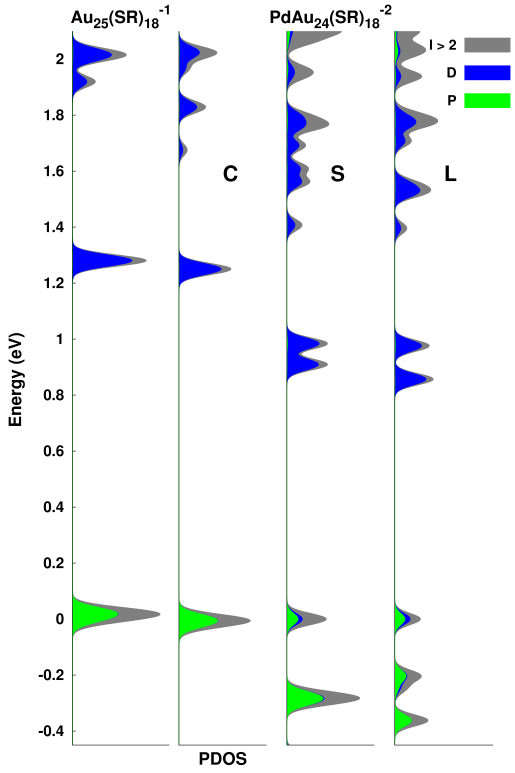

Figure 3.5: The Kohn-Sham electronic structure near the HOMO - LUMO gap for the closed-shell $Au_{25}(SR)_{18}^{-}$ and C, S and L isomers of $PdAu_{24}(SR)_{18}^{-2}$. PDOS denotes the angular-momentum projected density-of-states weights (PDOS) inside the metallic core. The color-filled curves denote thus weights of the KS orbital decomposition on spherical harmonics separated by their degree l=0,1,2 or (S, P, D). Gray denotes the sum of higher angular momentum components so that the sum of all the colors represents the total PDOS. The HOMO energy is set at zero. Note the similarity of the HOMO - LUMO gap and the character of the states in $Au_{25}(SR)_{18}^{(-1)}$ and C isomer of $PdAu_{24}(SR)_{18}^{(-2)}$ and the large disturbance by Pd in the electronic structure of S and L isomers of $PdAu_{24}(SR)_{18}^{(-2)}$.

very similar character of the electronic structure with the same HOMO-LUMO gap of 1.25 eV for the Pd-doped and undoped cluster. This leads to a conclusion that the C isomer of $PdAu_{24}(SR)^{-2}_{18}$ is clearly a doped complex derived from the eight-electron $Au_{25}(SR)^{-1}_{18}$ superatom. Substitution of a gold atom on the core surface or the ligand shell with Pd atom changes the electronic structure appreciably. The degeneracies of the HOMO and the LUMO states are split, although similar angular momentum features (compared to the C isomer) remain. The HOMO states split into two groups (degeneracies one and two) within 0.3 eV in the S isomer. In the L isomer, the three P-like states spread over 0.4 eV. The D-like LUMO is a 0.1 eV split doublet for both S and L isomers. The Kohn-Sham HOMO-LUMO (HL) energy gap calculated with PBE functional are found to be 1.25 eV, 0.91 eV, and 0.86 eV for C, S, and L isomer. For comparison, the HL gap from LB94 functional are 1.37, 1.11 and 1.05 eV for C, S, and L respectively. These details are clearly reflected in the respective optical spectra where new transitions are seen in the energy range of 1 to 2 eV (Article II).

From the analysis of Bader charge in the Pd atom it can be concluded that the doping atom remains essentially neutral in all cases, i.e., in C, S and L isomers in their various overall charge states. Thus, the Pd atom is inert or zero-valence with respect to donating or accepting charge to/from the superatom orbitals. In addition, the charging properties of $Au_{25}(SR)^{z}_{18}$ and the C, S and L isomers of $PdAu_{24}(SR)^{z}_{18}$ (Figure 4 in Article II) show the classical capacitive charging behaviour:

$$E(z) \propto z^2 \tag{3.5}$$

with deviations of the energies at z=-2 for $Au_{25}(SR)^{-1}_{18}$ and z=-3 for $PdAu_{24}(SR)^{-z}_{18}$. These deviations reveal the existence of a HOMO-LUMO gap at z=-1 and z=-2 as such a gap is crossed by varying the electron count.

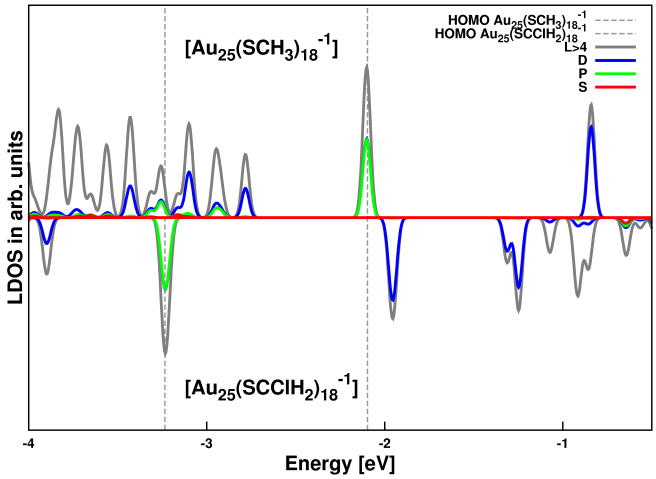

Figure 3.6: The projected local density of electron states (Kohn-Sham orbitals) in the frontier orbital region for the all-methylthiolate-passivated Au_{25} (upper panel) and for a cluster where all the ligands are chlorinated (bottom panel). The angular momentum character of the Kohn-Sham orbitals is analyzed by a projection onto spherical harmonics, centered at the cluster center of mass, and with a radius that encompassed the Au_{13} core. The major components of the angular momentum (L) analysis are shown by the colored lines up to L=2 (D-symmetry). The grey line denotes all the higher components L>2. The metal-electron shell structure (8 electron closed-shell configuration) of the Au_{13} core is not disturbed by the chlorinated ligands.

3.2.2 Doping the Ligand Shell by Chlorine

The motivation to study the ligand exchange reaction was guided by the previous observation [61], where fully exchanged $Au_{25}(SPhX)_{18}$ nanoparticles exhibit the redox formal potential shifts in the nuclear magnetic resonance spectroscopy (NMR) and electrochemical experiment. Moreover, in the completely exchanged nanoparticle ($Au_{25}(SPhX)_{18}$), the more electron withdrawing substitutions induced substantial changes of the HOMO and the LUMO energies, making the oxidation process more difficult. The goal was to understand changes in energy levels, the band gap and the charge distribution as a function of the number of ligands exchanged. A series of a ligand exchange reaction, where the original ligand was $-SCH_3$ and the incoming thiolate was $-SCH_2Cl$ were modelled to calculate the charge density re-distribution among the gold core, the semi-rings, and the electron withdrawing ligands.

A systematic replacement of the methylthiolate ligands in the $Au_2(SCH_3)_3$ "semi-rings" with the corresponding chlorinated ones was performed giving a composition $Au_{25}(SCH_3)_{18-x}(SCH_2Cl)_x^-$ with $0 < x < 18$. As it is shown in Figure 3.6 the character of the frontier orbitals indicates that for any x the $Au_{25}(SCH_3)_{18-x}(SCH_2Cl)_x^-$ clusters remain 8 electron "superatoms" with the HOMO-LUMO gap at 1.25 eV. Both HOMO and LUMO states are stabilized as a function of x in a rather linear fashion shown

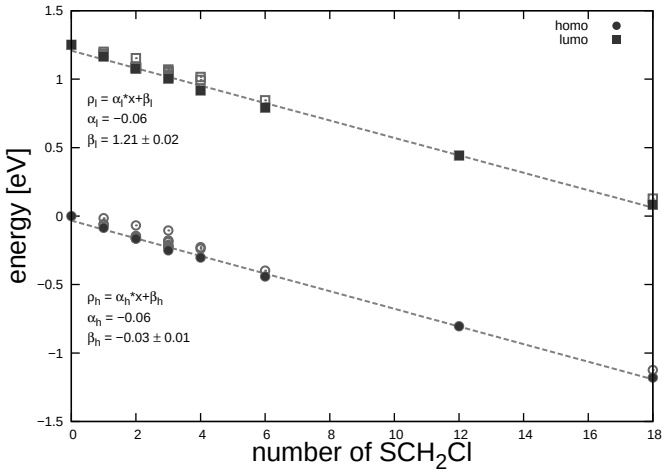

Figure 3.7: Energies of the HOMO and LUMO states as a function of chlorinated ligands in the model cluster $Au_{25}(SCH_3)_{18-x}(SCH_2Cl)_x^-$. The solid symbols correspond to the HOMO and LUMO energies of the optimal-energy isomers at a given x and the open symbols are the HOMO and LUMO energy of higher energy isomers. The HOMO-LUMO gap remains constant, but both HOMO and LUMO energies shift downwards (are stabilized) with the increasing number of SCH_2Cl.

in Figure 3.7. The downshift of the orbital energy is about 0.06 eV per each added SCH_2Cl.

The charge density analysis plotted in Figure 3.8 suggests no significant changes in the Au_{13} core of any chlorinated cluster, and the charge is rather transferred inside the semi-rings of ligands, mostly from the nearest-neighbour atoms. In the completely chlorinated cluster $Au_{25}(SCH_2Cl)_{18}^-$ the chlorine atoms attract a total negative charge of -4.42 |e| (-0.246 |e| per Cl), which originates from the 12 Au atoms in the semi-rings (total of +0.36 |e|), sulfurs (+0.94 |e|), and CH_2 groups (+3.12 |e|). This strong charge-transfer inside the semi-rings induces a strong modification of the electric dipoles in the ligand shell (shown in Figure S-8 in the Supporting Information of Article IV) which are responsible for the stabilization of the metal electron states of the Au_{13} core.

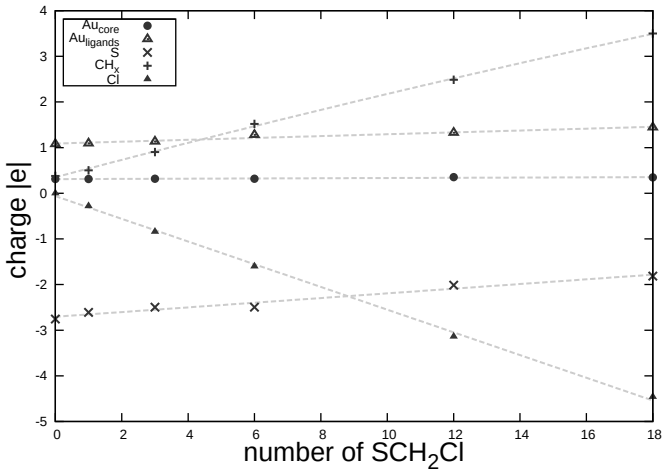

Figure 3.8: Bader charges (in |e|) versus number of exchanged ligands in the model cluster $Au_{25}(SCH_3)_{18-x}(SCH_2Cl)_x^-$. The Au_{13} core remains at the same weakly positively charge state as in the non-chlorinated cluster (with x=0). The total Cl charge (negative) increases linearly with x. The charge is depleted from the Au and S atoms and the CH groups in the gold-thiolate units ("semi-rings").

3.2.3 Undoped and Doped $Au_{25}(SR)_{18}^-$ Dimer

Early theoretical work on "magic" metal clusters explained the stability and nature of these systems in the context of the electronic shell model and suggested applications as possible building blocks for cluster-based materials [62]. Monolayer or multilayer nanoparticles films based on ligand/metal ion/metal linkers have already been produced by a variety of experimental methods in the past [63], and interesting properties, such as electronic conductivity, were observed and studied [64–66]. In this thesis, dimeric units linked together by benzene dithiolate (BDT) $[Au_{25}(SMe)_{17} - BDT - (SMe)_{17}Au_{25}]^{-2}$ are investigated, and the recent experimental and theoretical research on doped monolayer protected clusters motivated further studies on the substitution of certain atoms in one or two units [67]. The magnetic and non-magnetic transition metal atoms are considered in order to analyse the properties of the system. A center gold atom of the core of a subunit is replaced by a palladium atom $[PdAu_{24}(SMe)_{17} - BDT - (SMe)_{17}Au_{25}]^{-1}$ or a manganese atom $[MnAu_{24}(SMe)_{17} - BDT - (SMe)_{17}Au_{25}]^{-1}$, and later both center gold atoms are substituted by two manganese atoms $[MnAu_{24}(SMe)_{17} - BDT - (SMe)_{17}Au_{24}Mn]^0$.

The first considered system is a dimeric monolayer protected cluster cross-linked with the BDT written as $[(Au_{25}(SCH_3)_{17})_2S_2C_6H_4]^{-2}$ or as $[(Au_{25}(SCH_3)_{17}) - BDT - (Au_{25}(SCH_3)_{17})]^{-2}$, and the relaxed structure is shown in Figure 3.9. Due to the presence of the linker each unit of the structure is slightly deformed. The distance between two sulfurs that are perpendicular to the long axis of the dimer is shorter by 0.2 Å

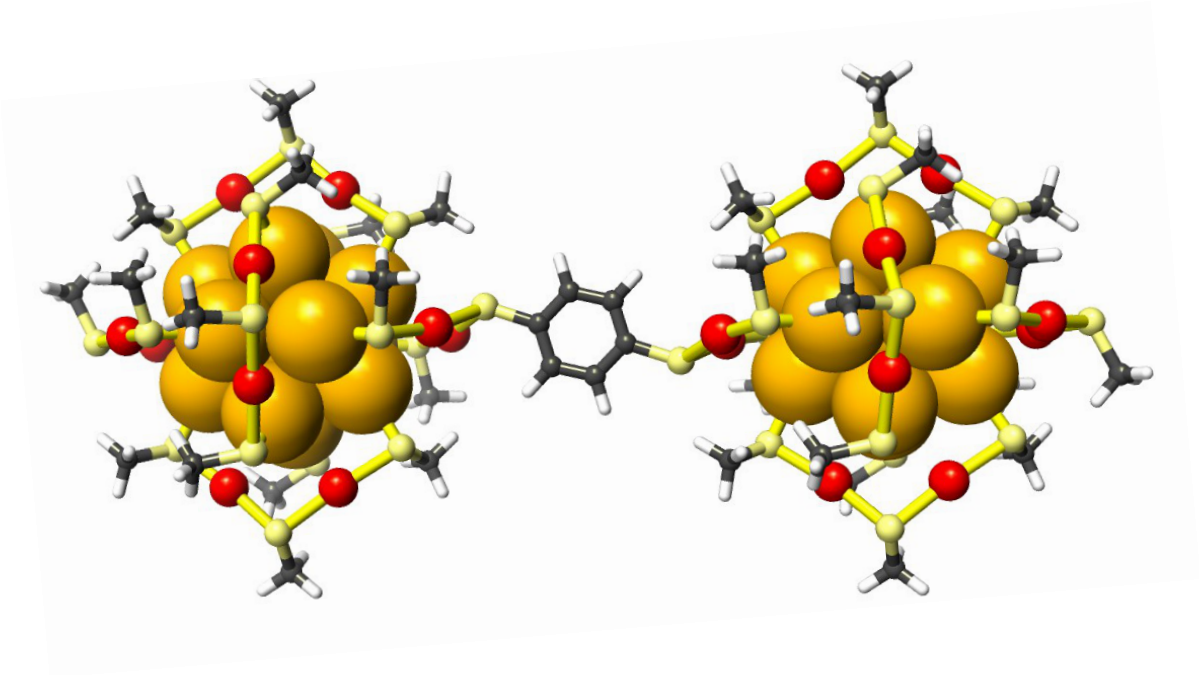

Figure 3.9: The structure of the relaxed dimer 3. Color code: Au^0 is yellow, S is lemon yellow, Au^I in the ligands is reddish, C is black, and H is white. Additionally, the methyl groups are shown by the sticks.

than the distance between two sulfurs of the same unit that lay along this axis. The small deviation is also pronounced in the angle between atoms that belong to the same ligand: the S-S-S angle increases from 102° to 107° and the Au-S-Au angle decreases 101° to 98°. The electronic structure analysis reveals that the HOMO-LUMO gap remains 1.25 eV and is the same as for the isolated $Au_{25}(SMe)^{-1}_{18}$. Additionally, each monolayer protected unit fulfils the so-called 8 electron "superatom" count with q=-1, where the electrons occupy twelve P-like orbitals of the HOMO level, and ten D-like empty orbitals are split in two groups by the octahedral ligand field, with four-fold LUMO and six-fold LUMO+1 shown in the upper Figure 3.10.

It was shown in Section 3.2.1 that the $PdAu_{24}(SR)^{q}_{18}$ cluster has a closed 8-electron superatomic shell structure when q = -2, and the Pd atom act as a zero-valent dopant [Article II]. Therefore, a Pd-doped dimeric MPC with a total charge q = -1 was expected to comprise a dimer of a "6-electron" superatom linked to an "8-electron" superatom, and is defined as $[PdAu_{24}(SMe)_{17} - BDT - (SMe)_{17}Au_{25}]^{-1}$. Figure 3.10 presents the projected local density of electron states in the frontier orbitals for each MPC unit analysed separately inside each core. It proves that the $PdAu_{24}(SCH_3)_{17}S$ is indeed a "6-electron" system with 2 electron absent from the P-like LUMO states (in Figure 3.11), which are separated by a rather small energy gap (0.2 eV) from the HOMO manifold. In contrast, the $Au_{25}(SCH_3)_{17}S$ cluster remains a closed shell "8-electron" superatom system.

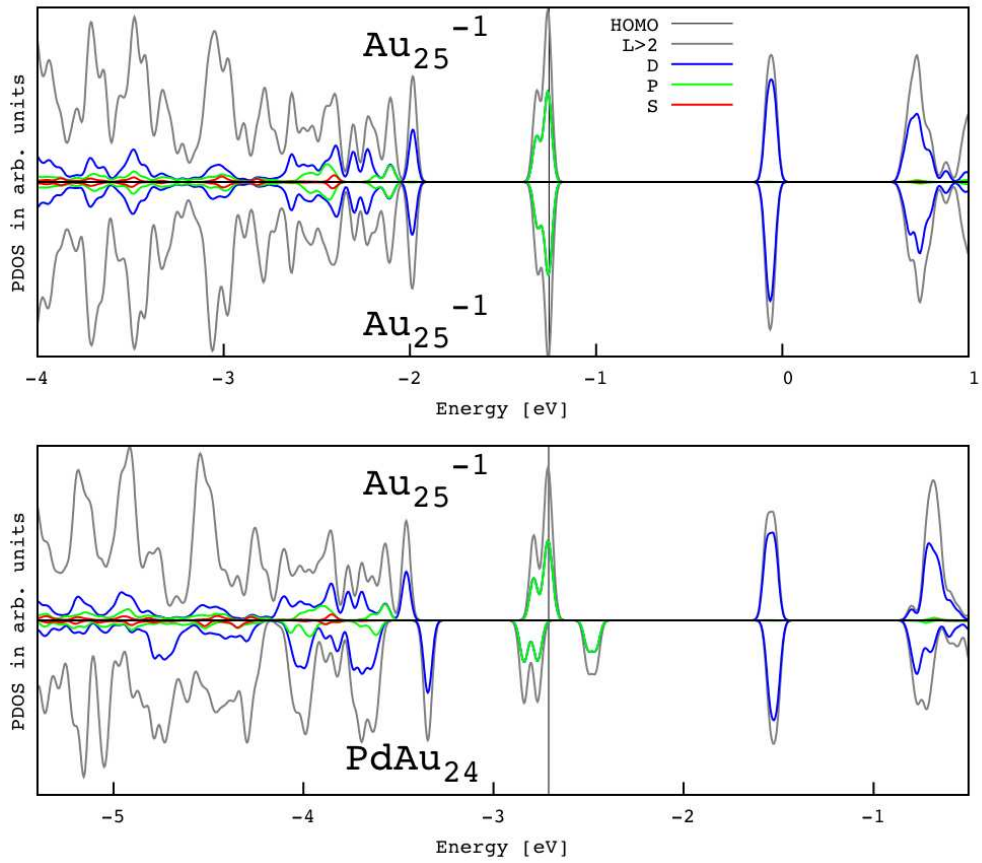

Figure 3.10: The electron density of states and its projections onto spherical harmonics (L = 0,1,2). The analysis is made with respect to the central atoms of the constituent clusters but with a radius that includes the 13-atom metal core. Upper figure displays analysis for $[(Au_{25}(SCH_3)_{17}S)2C_6H_4]^{-2}$ and lower for $[(PdAu_{24}(SCH_3)_{17}S) - C_6H_4 - (Au_{25}(SCH_3)_{17}S)]^{-1}$.

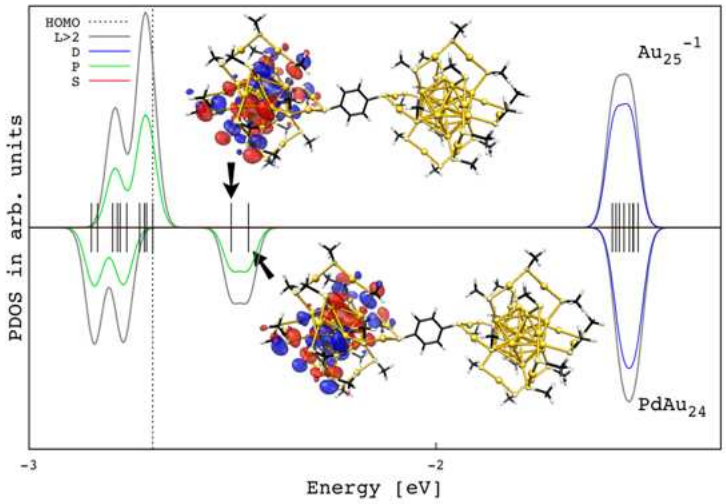

Figure 3.11: The electron density of states of dimer 4 and its projections to spherical harmonics (L = 0,1,2). The superatomic electron count is 14, and the dimer can be understood to compose of a closed-shell Au_{25}^{-1} and a 6-electron $PdAu_{24}$ with two holes in the P-like shell of $PdAu_{24}$. The hole states are visualized.

The last doping simulation was done by replacing the center atoms of the core of each MPC unit by one or two manganese atoms. Previous theory work [67, 68] has shown that the Hund's rule maximizing the spin multiplicity of nd-metal atoms in vacuum is not violated, if those metals are used as dopants at the center of the thiolate-protected $Au_{25}(SR)_{18}^{-}$ particle. Here, the interaction of the magnetic and non-magnetic parts and a paramagnetic configuration of the system are studied. The constructed $[MnAu_{24}(SMe)_{17} - BDT - (SMe)_{17}Au_{25}]^{-1}$ dimeric cluster is an "8-electron" magnetic superatom linked to an "8-electron" non-magnetic superatom. Left part of Figure 3.12 displays no changes in the electronic structure of the non-magnetic unit in the presence of magnetic species. The character of the frontier orbitals (P-type HOMO and D-type manifold of empty states) and the HOMO-LUMO gap remain the same. In the magnetic part, new (empty) states appear just above the HOMO manifold of the dimer, separated by less than 0.1 eV from the HOMO. Analysis of different spins, and the local analysis around the Mn atom confirm that these states are the empty spin-β $3d$ states of Mn, while the occupied spin-α $3d$ states are found in the range of 2 - 2.5 eV below HOMO, strongly hybridized with the Au $5d$ band. The calculated magnetic moment for the dimer is 4.6 μB, and the moment is concentrated on Mn. Qualitatively, the electronic structure of the $MnAu_{24}(SMe)_{17}$ part of the dimer remains very much the same as was recently shown for a single $MnAu_{24}(SMe)_{18}$ cluster [67]. The right part of Figure 3.12 shows the electronic structure of the double-doped dimer $[MnAu_{24}(SMe)_{17} - BDT - (SMe)_{17}Au_{24}Mn]^{0}$ in a ferromagnetic state. Magnetic units remain independent from each other with unpaired spins aligned in one direction and localized around each manganese.

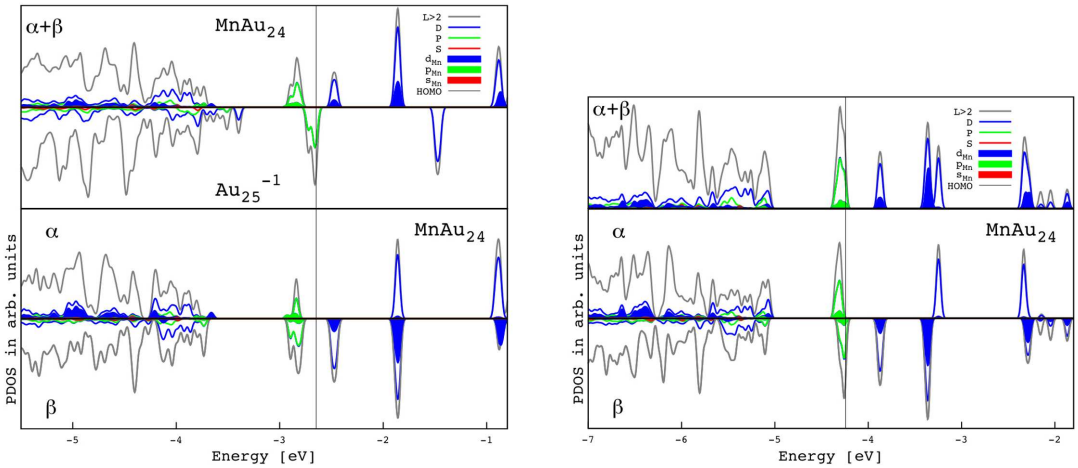

Figure 3.12: The electron density of states of magnetic dimers. On the left: $[MnAu_{24}(SMe)_{17} - BDT - (SMe)_{17}Au_{25}]^{-1}$, and on the right: $[MnAu_{24}(SMe)_{17} - BDT - (SMe)_{17}Au_{24}Mn]^{0}$. Top left figures displays PDOS separately for each unit summed over the spin. Top right: summed PDOS over magnetic cores. Symbols α and β indicate analysis over different spin states. Projections onto spherical harmonics ($L = 0,1,2$) are made with respect to the central atoms of the constituent clusters but with 4 Å radius which encloses the 13-atom metal core.

As a summary, analysis of the electronic structure and magnetic properties indicates that dimeric monolayer protected clusters behave truly as dimers of two independent clusters, even if one introduces impurities inside the metallic core. This conclusion suggests that cross-linked clusters in solution might have similar ratio between charge/mass as the single units, and therefore it might be difficult to distinguish whether experimental solution contains linked or separated clusters.

3.3 Catalysis on Small Gold Clusters

Studying catalysts and catalytic processes was accelerated by the systematic research conducted by Jöns Jacob Berzelius [69], and later by the need for industrial applications [70]. Berzelius described reactions that are accelerated by substances that remain unchanged after the reaction, using the word *catalysis* [71]. In other words, a catalyst provides an alternative reaction, which lowers the activation energy. Catalytic reactions on surfaces are classified as Langmuir-Hinshelwood (L-H) or Langmuir-Rideal (Rideal-Eley) (E-R) mechanisms. L-H reaction occurs between species that are adsorbed on the surface, and E-R reaction takes place between a reactant molecule in the gas phase and another one that is adsorbed on the surface. Another basic concept related to an elementary reaction is the Arrhenius law, which states that:

$$\frac{d}{dT}\ln k(T) = \frac{E_a}{RT^2}, \tag{3.6}$$

where k is the reaction rate, E_a is the activation energy of the reaction, R is the gas constant, and T is the temperature. This leads to an exponential law:

$$k = Ae^{-\frac{E_a}{RT}}, \tag{3.7}$$

which can be used to estimate the probabilities of given reactions. The pre-exponential factor A is usually taken to be the order of typical vibration frequencies (10^{13} 1/s).

This thesis focuses only on the reactions catalyzed by gold clusters and the intellectual progress and specific achievements that have resulted in during the long history of research on catalysis have been discussed in many books and review articles.

Gold was not considered as a potential catalyst for many centuries, mainly due to the fact that it requires specific conditions under which it manifests catalytic activities. Gold in bulk is completely inactive but in finely dispersed form it is very active. However, already in the beginning of 20th century (1906) the oxidation of hydrogen on gold was observed. The earliest reference to gold as a catalyst for carbon monoxide oxidation dates to 1925 [72]. During the 1970's, two brands of catalytic gold research were recognized. One focused on gold supported on alumina and silica, and the other examined gold metals with rare gases at low temperature (-263°C) [73]. In 1980's, nanometer-sized gold particles where considered as potentially important in catalytic applications [62, 74, 75]. The breakthrough arrived with the seminal studies of M. Haruta, where the adsorption properties and reactivities of gold complexes were summarized in terms of their size dependency from bulk to fine particles, clusters and

atoms [76]. Additionally, he identified the catalytic oxidation of carbon monoxide by the nano-sized gold particles on metal oxide at $-73°C$.

Next important subject that called for attention, was the question how is the oxygen molecule activated on the catalyst. The X-ray experiment with the high-energy-resolution fluorescence detected method (HERFD), which allows to observe the steps and paths of the reaction, determined that the oxygen molecule which is bound to the finely dispersed gold reacts with carbon monoxide to form carbon dioxide, and this reaction does not take place without Au nano-particles [77]. The reason for the low-temperature activity of nanoscale gold must be the ability to either effectively dissociate oxygen molecules with low activation barriers or at least bind an activated O_2^* species on the surface. Model-catalytic studies on CO oxidation over oxide-supported, size-selected small gold clusters point to the latter mechanism, where electron transfer from the support to the di-oxygen (through the gold cluster) activates it to peroxo- or superoxo-species [78–81]. Size-selected small thiolate protected gold clusters indicate a mechanism where electron transfer from the core of the cluster activates the superoxo-species. The mechanism is studied in the subsection 3.3.2 and in the article III. A significant influence in the reaction mechanism is the choice of a support material between the so-called "active" (or sometimes called "reactive") and "inert" oxide support. Active supports such as Fe_2O_3, NiO_x, CoO_x, or TiO_2 improve the activity of gold catalysts, while MgO, Al_2O_3 have a low ability to adsorb or store oxygen at low temperatures. Moreover, the catalyst activity strongly depends on the particle size (2 nm and below), when it is placed on an inert support [82–84]. This is not the case for the "active" support, where gold particles as large as 12 nm (Au/Fe_2O_3) or 30 nm (Au/TiO_2) oxidise carbon monoxide. Oxygen molecule adsorbs in large quantities on these "active" support materials as a O_2^* (O_2^-) species [85].

In the following subsections, L-H and E-R mechanisms are studied in order to gain insight into the catalytic properties of very small gold clusters and thiolate-protected superatom clusters. In the section 3.3.1 energetics and dynamical pathways of the L-H reaction for hydrogen peroxide formation from H_2 and O_2 bound to neutral gold tetramers have been investigated by applying two strategies: $T = 0$ K geometry optimizations and constrained Car-Parrinello molecular dynamics simulations at $T = 300$ K. Section 3.3.2 describes studies on the L-H and E-R mechanisms for oxidation of carbon monoxide on "9"- and "10"-electron superatoms using the GPAW code [86].

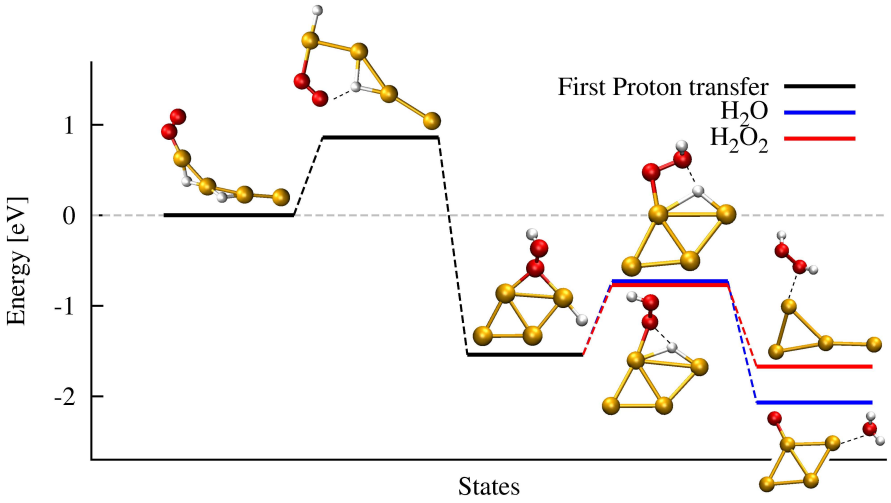

Figure 3.13: Optimized (0 K) configurations of the Au_4 catalyzed reaction and the corresponding differences in total energies. The two competing final states involve H_2O_2 and H_2O formation, respectively. The TM geometries have been obtained from the 300 K simulation by performing P-RFO search near the transition points, except the one for H_2O formation which is based on a separate GO simulation with P-RFO. Colour code: gold, yellow; oxygen, red; and hydrogen, white.

3.3.1 H_2O_2 Formation

The presence of hydrogen peroxide was first reported by a French chemist Louis-Jacques Thenard in 1818, as a natural metabolite of many organisms. Hydrogen peroxide is an environmentally-friendly and one of the most powerful oxidizers known up-to-date. H_2O_2 based disinfection can be used as a method of therapy as long as it is used in a non-toxic concentration [87]. Structure of the molecule is very similar to the structure of water molecule, but it is less stable. H_2O_2 is colourless, odourless, oxidizer liquid, which has to be stored under proper conditions to prevent explosive reactions with combustibles. Often, it is used in a water solution as a bleaching and antiseptic agent. The need of H_2O_2 is very high, since it is used as a bleach in the pulp and paper industry and in the treatment of waste water [88]. In addition, it was proved that H_2O_2 effectively removes residual aromatic sulfur compounds from fuels [89]. Therefore, it is necessary to design catalysts which form H_2O_2 and minimize the decomposition into H_2O. The high demand on finding an alternative "green chemistry" method to the current technology has resulted in many studies on the direct formation of H_2O_2 from H_2 and O_2 over supported Au, Pd and Au-Pd nanoparticles [90–93].

This sub-section focuses on the dynamics of the competing reaction channels for water and hydrogen peroxide formation. In each case, the reaction barriers for Au cluster catalysed proton transfer are less than 1 eV. Water formation is a competitive reaction

channel, and the relative weight of H_2O and H_2O_2 products may depend on the chosen Au cluster size. Molecular dynamic simulations demonstrate the significance of the geometric fluxionality of small catalytic Au clusters. In Article I, two methods were presented, and both metadynamic and constrained MD simulations show significant fluctuations of the Au cluster during the course of the reactions. An extreme example was provided by the occurrence of dynamic insertion of di-oxygen between the Au atoms in Au_2 dimer (Figure 2 in Article I). These studies suggest that neutral Au clusters could work as catalysts in aerobic H_2O_2 formation in ambient conditions.

The ground state geometry of the Au_4 cluster is a rhombus. However, this changes upon binding with H_2 and O_2, and the initial state comprises a linear gold tetramer. As a preliminary step, again, the H dimer has dissociated on Au with a reaction barrier of 0.50 eV, and the oxygen dimer (singlet) binds to a peripheral Au atom (Au-O distance 2.07 Å). The total energy of the system is 0.15 eV higher than that for the separated reactants (Au_4, O_2 (triplet) and H_2).

The elementary steps in the direct H_2O_2 formation in the presence of an Au cluster can lead to two competing channels, with H_2O_2 and H_2O as end products.

Channel I:

$$H_2 + O_2 + Au_N \longrightarrow H_2O_2 + Au_N \tag{3.8}$$

Channel II:

$$H_2 + O_2 + Au_N \longrightarrow H_2O + Au_NO \tag{3.9}$$

$$H_2 + Au_NO \longrightarrow H_2O + Au_N \tag{3.10}$$

The first reaction was conducted at 0 K using geometry optimization and is shown in Figure 3.13. The first transition state (TS) appears in the nearly planar configuration, O_2 is tilted and points to the proton (O-H distance 1.98 Å) that is connected to two Au atoms. The corresponding energy barrier is 0.86 eV. After this stage, the Au cluster recovers its initial rhombus geometry, and the formed hydroxyperoxy intermediate connects two Au atoms (distances 2.95 Å) with the transferred H pointing outwards. The corresponding energy change with respect to the initial state is -1.63 eV. The second proton transfer leads to two alternative final states, with (a) hydrogen peroxide and (b) water formation, for which the reaction barriers at 0 K are 0.77 eV and 0.81 eV, respectively, and the TS geometries display obvious similarities: both involve a rhombus-like Au_4H which is in contact (obtuse corner) with the unsaturated oxygen, and the O-H distances are 1.74 Å and 1.67 Å, respectively.

The total energies of the final configurations are -1.67 and -2.07 eV, respectively. The former involves a Y-shaped Au_4 isomer with an Au-O contact with H_2O_2 (2.24 Å, Au_4/H_2O_2 binding energy 0.57 eV). The latter end configuration comprises a rhombus-like Au_4O which binds to water oxygen (2.30 Å, Au_4O/H_2O binding energy 0.62 eV).

The upper image in Figure 3.14 shows the reaction path at 300 K. Molecular dynamics was executed with 0.0726 fs time steps and the fictitious electron mass was set to 400 m_e in the coupled Lagrange equations of motion for the ions and electrons. The constrained molecular dynamics used 2 ps time intervals (27 561 steps each) for each reaction step. Distance H(1)-O(1) of the initial state is chosen as the reaction coordinate which is gradually reduced until a covalent O-H bond is formed (proton transfer). For the first proton transfer, E_{pot} increases steadily and the reaction barrier of 0.95 eV is found at 1.75 Å. This should be compared with the 0 K transition state in Figure 3.13, where the barrier height is slightly lower, and the reaction involves an isomerisation of Au_4 (rhombus). The resulting intermediate state is 1.48 eV below the starting level. For the second proton transfer, Channel I initiates a reaction from the intermediate state with another constraint H(2)-O(2). Reduction of this distance (Channel I, middle Figure 3.14) leads to a gradual increase in E_{pot} as the unsaturated oxygen and hydrogen approach, and the reaction displays a preliminary barrier of 0.82 eV at 2.86 Å that does not involve changes in chemical bonding. The atomic trajectory reveals that this is caused by a steric effect: O and H are now on the opposite sides of a sharp Au corner, and they have to be displaced out of the rhombus plane in order to get closer. The actual reaction barrier for the second proton transfer (0.71 eV) follows at 1.80 Å corresponding configurations similar to TS in Figure 3.13, and the resulting final state involves a Y-shaped gold tetramer in contact with hydrogen peroxide. The averaged potential energy of the end-configuration is 1.63 eV lower than in the beginning.

Similarly, Channel II initiates a reaction from the intermediate state with a constraint H(2)-O(1). At 0 K, reduction of this distance leads to formation of a metastable oxo-water and E_{pot} increases significantly. The complete formation of a water molecule requires an additional O-O stretching, and the high energy barrier and the unfavourable end-product demonstrate the failure of this approach.

At 300 K, Channel II (lower Figure 3.14) shows a considerably different reaction path than the 0 K simulation. Reaction barriers are observed at 2.54 Å (0.68 eV) and 1.75 Å (0.60 eV) corresponding to changes of the gold cluster. The first barrier appears when the gold tetramer has to be displaced out of the plane to provide an opportunity for the proton to conquer the sharp corner of the cluster. The next barrier is associated with the O-H bond formation and involves fluctuation of the Au tetramer between the Y-shaped and rhombus isomers. The Au-Au bond, which is initially in contact with the OOH^- radical, varies between 2.8-5.0 Å. Additionally, a metastable oxo-water is created after the second reaction barrier which spontaneously dissociates as the

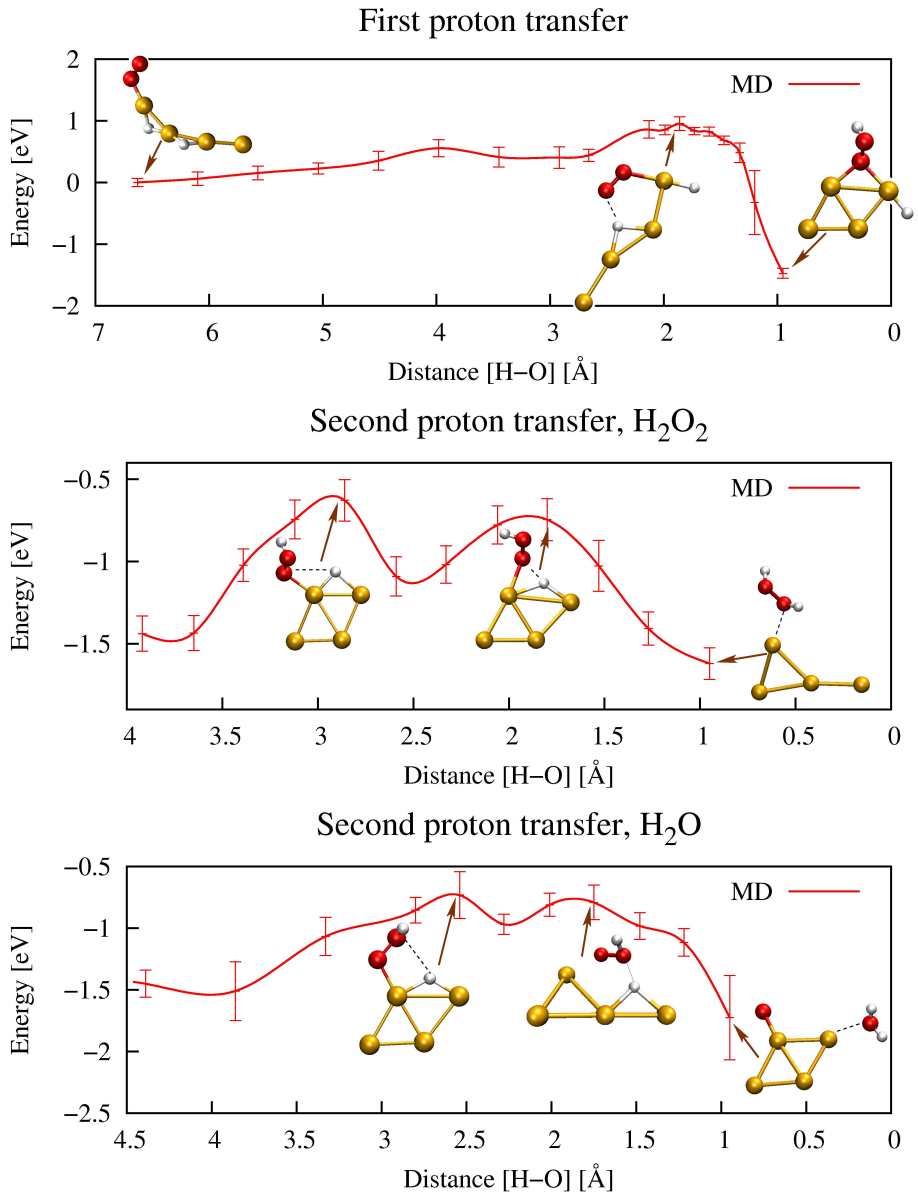

Figure 3.14: Reaction paths of the Au_4 catalyzed reactions at 300 K as a function of constrained distance and potential energy (error bars correspond to standard deviation). Upper image: first proton transfer; middle image: second proton transfer (Channel I), where the end products are hydrogen peroxide and Au_4; lower image: second proton transfer (Channel II), where the end products are water and Au_4O.

reaction proceeds. Finally, the formation of a water molecule yields a potential energy of -1.73 eV with respect to the initial state, and the final configuration comprises a rhombus-like Au_4O in contact with H_2O. The Au_4O cluster can now react with a additional H_2 in order to complete the reaction cycle of Eqs. 3.8-3.9.

Referring to the equation 3.7, it is estimated that for the activation energy of 0.7 eV at 300 K temperature with the frequency factor of 10^{13} 1/s, the rate constant k is about 17 reactions per second. Since the relationship between the activation energy and the average kinetic energy has exponential behaviour, higher activation energy for the reaction, for example 1 eV, decrease the rate constant practically to zero. Also, if one decreases the temperature down to 280 K with the activation barrier 0.7 eV, the reaction constant is about of 3 reactions per second.

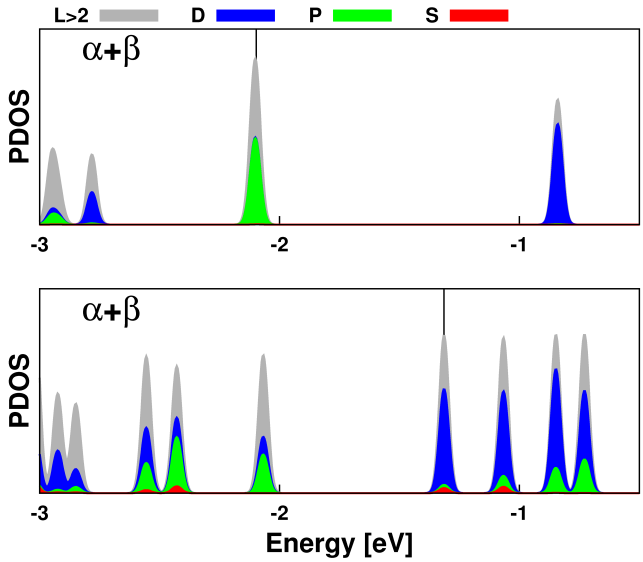

Figure 3.15: Projected density of states obtained by projection onto spherical harmonics inside the Au_{13} core. Figures show PDOS: on the top for "8"-electron $Au_{25}(SR)^{-}_{18}$, and on the bottom for "10"-electron $Au_{21}(SR)^{-}_{12}$. Both PDOS are summed over the spin α and β.

3.3.2 CO Oxidation

Carbon monoxide (CO) is formed by the incomplete combustion of any carbon substance, and it is odourless, colourless and poisonous gas. Development of highly efficient and eco-friendly materials, which enable to oxidise CO to CO_2 with a proper yield, is constantly needed. This study investigates the direct formation of CO_2 over partially protected gold clusters simulating E-R and L-H models. The reactivity of the cluster $Au_{25}(SR)^{-}_{18}$ is obtained by removing an $Au_2(SR)_3$ unit from the protecting shell. Thereby, the number of "metallic" electrons in the gold core increases by the number of removed ligands, and "9"- and "10"-electron systems are achieved by detaching one or two units, respectively.

Figure 3.15 shows the projected density of states of the "8" and "10"-electron systems. in the later, two "extra" electrons occupy states over an energy gap, which originate from the HOMO-LUMO gap of the fully protected parent cluster ("8" - electron system). When two units are removed from the "8"-electron cluster, the shell closing configuration $1S^2 1P^6$ with $1D^{10}$ lowest unoccupied states is modified to $1S^2 1P^6 1D^2$ with $1D^8$ lowest unoccupied states. Thus, two highest itinerant electrons occupy the D-symmetric states. Upon gradual adsorption of O_2 and CO, the electrons are transferred to one of the $2\pi^*$ orbitals, and this is described in Figure 3.16 and 3.17. To understand the nature of chemical bonding in this mechanism, the adsorption of oxygen molecule

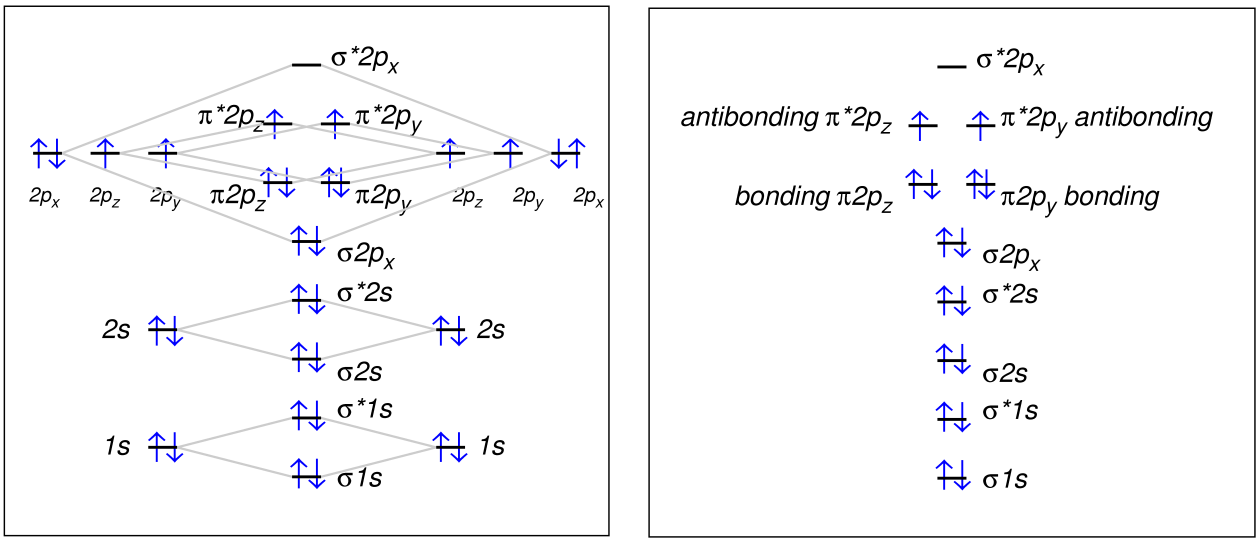

Figure 3.16: Oxygen molecule with two unpaired electrons in its triplet ground state.

on the partially protected cluster was studied.

Oxygen molecule is a species with two unpaired electrons in its ground state, as it is shown in Figure 3.16. The arrangement for these two electrons is related to the degeneracy of the electronic state calculated from 2S+1, where S is the total electron spin angular momentum. Therefore 2S+1 is equal to 3, since S=1 for two unpaired electrons with half spin. This makes the ground stated a triplet, where the $\sigma 2p_x$ bonding orbital is lower in energy than the πp_y and πp_z. Anti-bonding σ^* rises in energy above the Fermi level. The highest occupied molecular states $\pi^* p_y$ and $\pi^* p_z$ are occupied by two electrons with unpaired spins. Top left Figure 3.17 display the density of states around the oxygen dimer separated over the spin state α and β. Electrons with the same spin α occupy the HOMO state, while the electrons with the opposite spin β are localized in the LUMO state (the same as it is shown in Figure 3.16). Figure 3.17-A shows that the oxygen molecule adsorbed on a partially protected cluster, where it freely accepts an itinerant electron from the metallic core of this cluster in the lowest unoccupied molecular orbital of the neutral triplet of O_2. This means that the lowest unoccupied triplet state of the oxygen molecule becomes occupied, and the oxygen dimer is activated to the superoxo-state O_2^-.

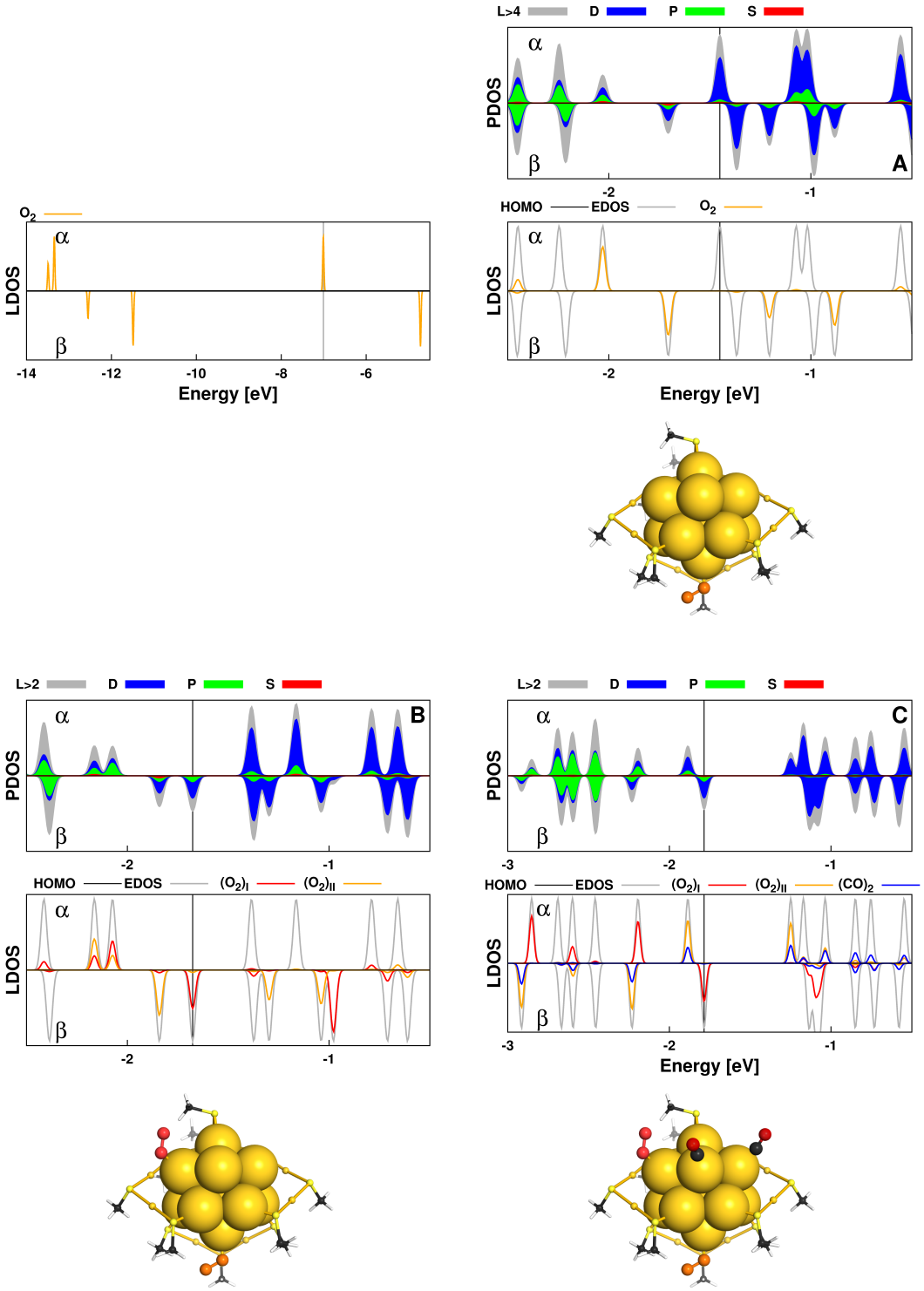

Figure 3.17: Top left Figure 3.17 displays the local density of states around the oxygen atoms in the O_2 molecule separated over the spin state α and β. Top figures A, B and C show the projected density of states projected onto spherical harmonics inside the Au_{13} core. Bottom figures A, B and C show the O_2 molecule, two oxygen molecules, and two CO and O_2 molecules adsorbed a partially protected cluster, respectively.

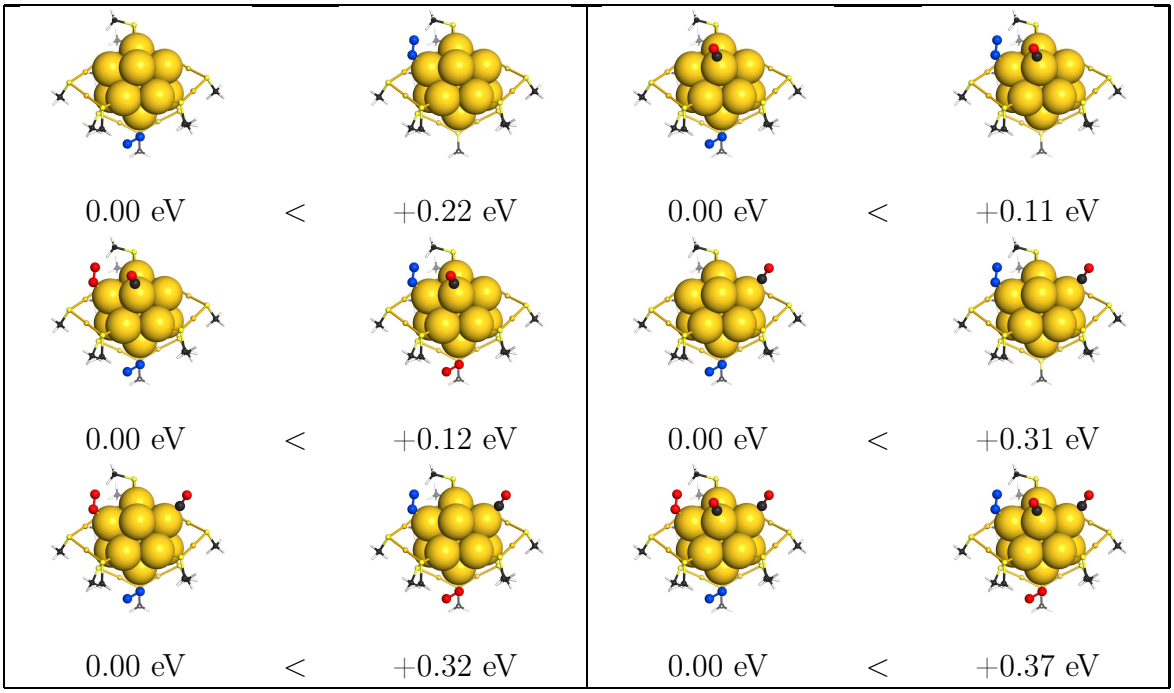

Figure 3.18: The relative binding energies of the O_2 molecule. The molecule adsorbed onto the gold cluster is coloured in blue in order to distinguish it from the molecules which are already bound to the cluster.

The binding energies of O_2 to "9"- and "10"-electron systems are very similar, which was expected due to the symmetric shape of the core, and the energies are defined as:

$$\Delta E = E[Au_{23}(SMe)_{15}(O_2)^{-1}] - E[O_2] - E[Au_{23}(SMe)_{15}^{-1}] \tag{3.11}$$

$$\Delta E = E[Au_{21}(SMe)_{12}(O_2)_2^{-1}] - 2 * E[O_2] - E[Au_{21}(SMe)_{12}^{-1}] \tag{3.12}$$

and they are 0.72 eV and 0.62 eV/O_2 for the "9"- and "10"-electron system, respectively. However, it has been shown that the binding energy of the oxygen molecule depends on the local environment [94]. This is also well pronounced in the "10"-electron system of the thiolate-protected gold cluster which has 4 non-equivalent binding sites: three nearest-neighbouring unprotected Au atoms and one exposed Au atom on the opposite side of the core. Figure 3.18 displays the relative binding energies of the oxygen molecule. The molecule adsorbed onto the gold cluster is coloured in blue in the figure 3.18 in order to distinguish it from the molecules which are already bound to the cluster.

Adsorption of O_2 on a single-exposed gold atom is favoured over adsorption on one of the three unprotected gold atoms by 0.2 eV. The cluster becomes anionic in the

presence of two O_2 molecules, and adsorption to the sites that are nearest neighbours is strongly unfavourable due to the repulsion between these molecules. CO/CO_2 oxidation exhibits also coverage-dependent reactivity and that has already been observed [94]. The binding energy per O_2 molecule varies within 0.4 eV when neighbouring sites are occupied by CO, because CO molecules rearrange molecular orbitals of the adsorbed O_2 as it is shown in bottom right Figure 3.17-B,-C. It is important to remark that the number of O_2 molecules that a given cluster is able to bind and activate to the superoxo-state is determined by the number of itinerant electrons that occupy the highest-energy levels over the HOMO-LUMO gap of the initial cluster. In turn, this is dictated by the number of removed electronegative ligands from the parent cluster.

In this subsection, two mechanisms for CO oxidation are presented. One should mention that the reactions consider only O_2 adsorbed perpendicular to the surface of the core, since it was shown that the activation barrier is significantly higher when the O_2 molecule is adsorbed parallel to the Au surface with two Au-O bonds (Article III). In addition, calculated values for energy barriers are obtained using GGA (PBE) functional, since repeated calculations using Meta-GGA (TPSS) provided results that are typically within 0.1 eV (Article III). For the "9"-electron system, where one of the six protecting ligands is removed, L-H and E-R mechanisms are studied. The schemes for the reactions are presented below:

$$\mathrm{Au_{21}(SR)_{12}^{-} - O_2 + CO(g) \longrightarrow Au_{21}(SR)_{12}^{-} - O + CO_2(g)} \tag{3.13}$$

for the E-R reaction, and

$$\mathrm{Au_{21}(SR)_{12}^{-}CO - O_2 \longrightarrow Au_{21}(SR)_{12}^{-} - O + CO_2(g)} \tag{3.14}$$

for the L-H reaction. g denotes molecule in the gas phase. Figures 3.19, 3.20, 3.21 and 3.22 show the energy landscape and the configurations for the important intermediate metastable minima and transition states in the E-R and L-H reactions for the "9"- and "10"-electron systems.

The "9"-electron system is obtained by removing one ligand. Therefore, two gold atoms of the surface of the core are exposed. Initial configuration in Figure 3.19-a and 3.20-a represents complexes in the gas phase. Bader charge analysis reveals that upon adsorption of oxygen molecule charge of a 0.5 |e| is transferred from the cluster to O_2, and the oxygen dimer is activated to a superoxo-like state and the O-O distance increases from 1.24 Å to 1.31 Å. The distance between the gold atom from the core to the connecting oxygen atom is 2.22 Å.

Since the E-R reaction takes place between a reactant molecule in the gas phase and another one that is adsorbed on the surface carbon monoxide collides head-on with O_2. The intramolecular C-O distance is 1.15 Å in the gas phase. The transition occurs when the shortest distance between C atom from CO and O from O_2 is 1.69 Å (Figure 3.19-c), and the corresponding reaction barrier is 0.48 eV. The intramolecular O-O and C-O distances are slightly stretched to 1.36 Å and 1.18 Å, while the Au-O distance is 2.19 Å. Figure 3.19-d shows the intermediate state after which CO_2 is formed. The distance between the remaining O atom and neighbouring gold is 1.98 Å.

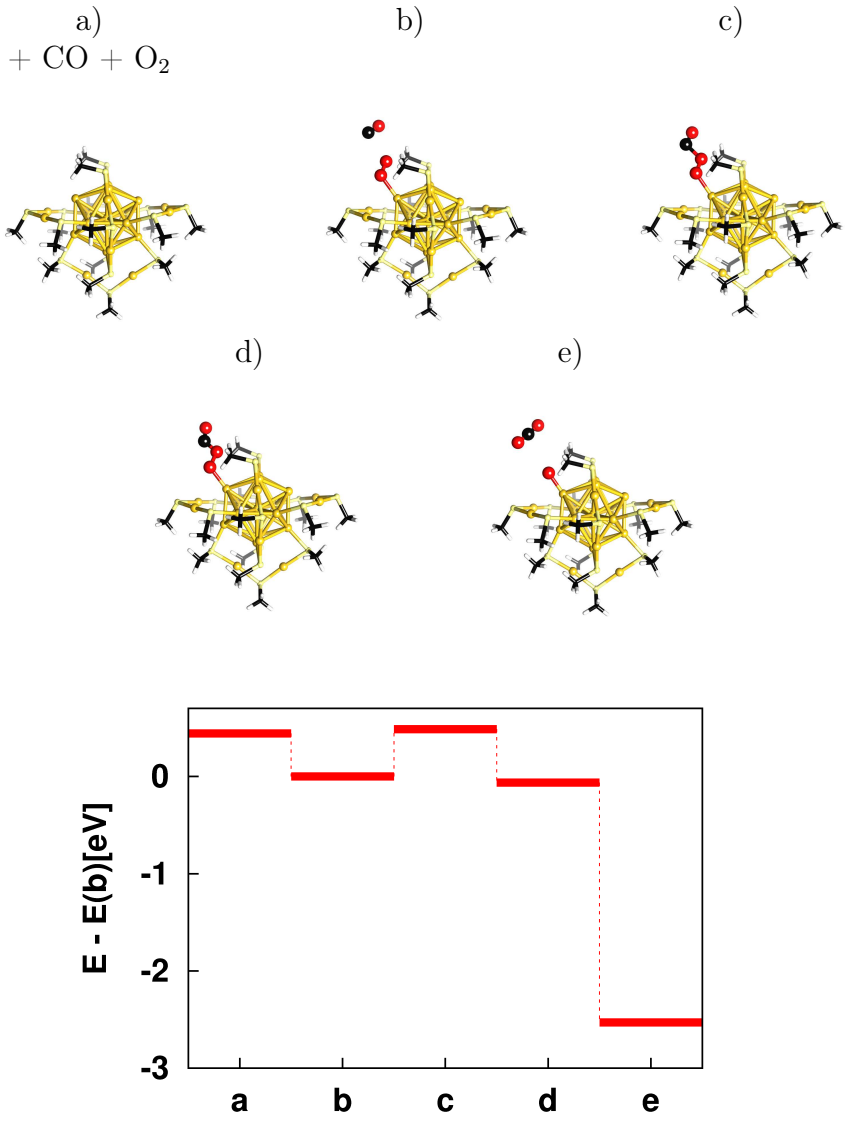

Figure 3.19: The energy landscape and the configurations for the important intermediate metastable minima and transition states in the E-R reaction for the "9"-electron systems.

The L-H reaction occurs between species that are adsorbed on a surface. In Figure 3.20-b the O_2 and CO molecules are adsorbed on the surface of the core. In this case, after removing a ligand the molecules occupy both exposed areas of the core. Again, the O-O distance of the adsorbed molecule is 1.31 Å, which indicates a superoxo-like state and the Au-O distance is 2.25 Å. The C-O distance is 1.15 Å and the C-Au distance is 1.98 Å. Figure 3.20 shows that two transition states have to be conquered to form carbon dioxide. The first transition occurs when the carbon monoxide occupies a three-fold hollow side on the gold surface and the shortest carbon-O_2 distance is 5.56 Å. The corresponding barrier is 1.56 eV. The intermediate state is lower in energy by 1.04 eV with CO on a Au-Au bridge at 3.50 Å distance from O_2. The second reaction barrier of 1.36 eV is associated with the C-O bond formation (2.05 Å distance between the atoms), and the Au-O distance is elongated to 2.35 Å. After the second reaction barrier, a metastable peroxyformate is created which spontaneously dissociates as the reaction proceeds. The reaction is not likely to occur due to the high activation barrier. This is consistent with the geometry analysis, which shows that the Au-S interface of the "9"-electron cluster has two exposed gold atoms on the core surface that are not nearest neighbours. Therefore, two $Au_2(SR)_3$ units have to be removed to expose two nearest-neighbour gold sites. Moreover, the first transition state for the reaction is higher than the total energy of the reactants in the gas phase. Although the activation energy of the E-R reaction is calculated to be 0.48 eV, the importance of such reactions is regarded to be smaller than the L-H reactions due to a smaller probability of head-on collision between the gas-phase and surface-bound reactants. Several previous studies have shown that CO_2 production is dominated by Langmuir-Hinshelwood mechanism [94].

For the "10"-electron system, two $Au_2(SR)_3$ ligands are removed in such a way, that two nearest-neighbours Au sites are exposed. These sites are occupied by two CO and two O_2 molecules. A two-stage reaction is provided:

Step 1:

$$Au_{21}(SR)_{12}^{-} - 2(CO_2) - 2(O_2) \longrightarrow Au_{21}(SR)_{12}^{-} - CO - O - O_2 + CO_2(g) \quad (3.15)$$

Step 2:

$$Au_{21}(SR)_{12}^{-} - CO - O - O_2 \longrightarrow Au_{21}(SR)_{12}^{-} - O_2 + CO_2(g) \quad (3.16)$$

The Figure 3.21 shows the energy landscape for the first step of CO_2 formation over the "10"-electron system (Eq. 3.15). Two CO_2 and one O_2 molecules are adsorbed on the three-fold exposed area of the core surface, and the remaining O_2 is adsorbed on

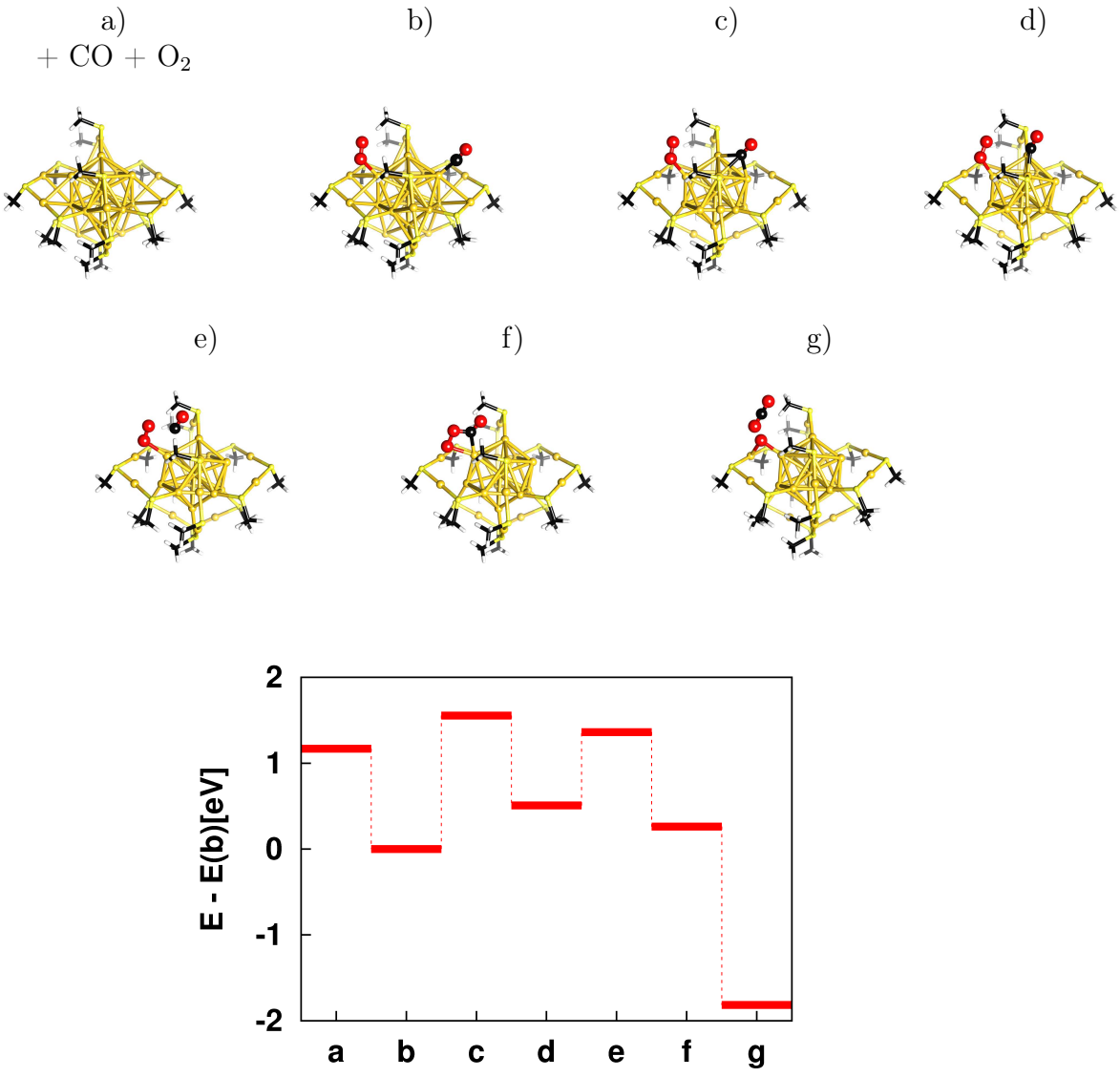

Figure 3.20: The energy landscape and the configurations for the important intermediate metastable minima and transition states in the L-H reaction for the "9"-electron systems.

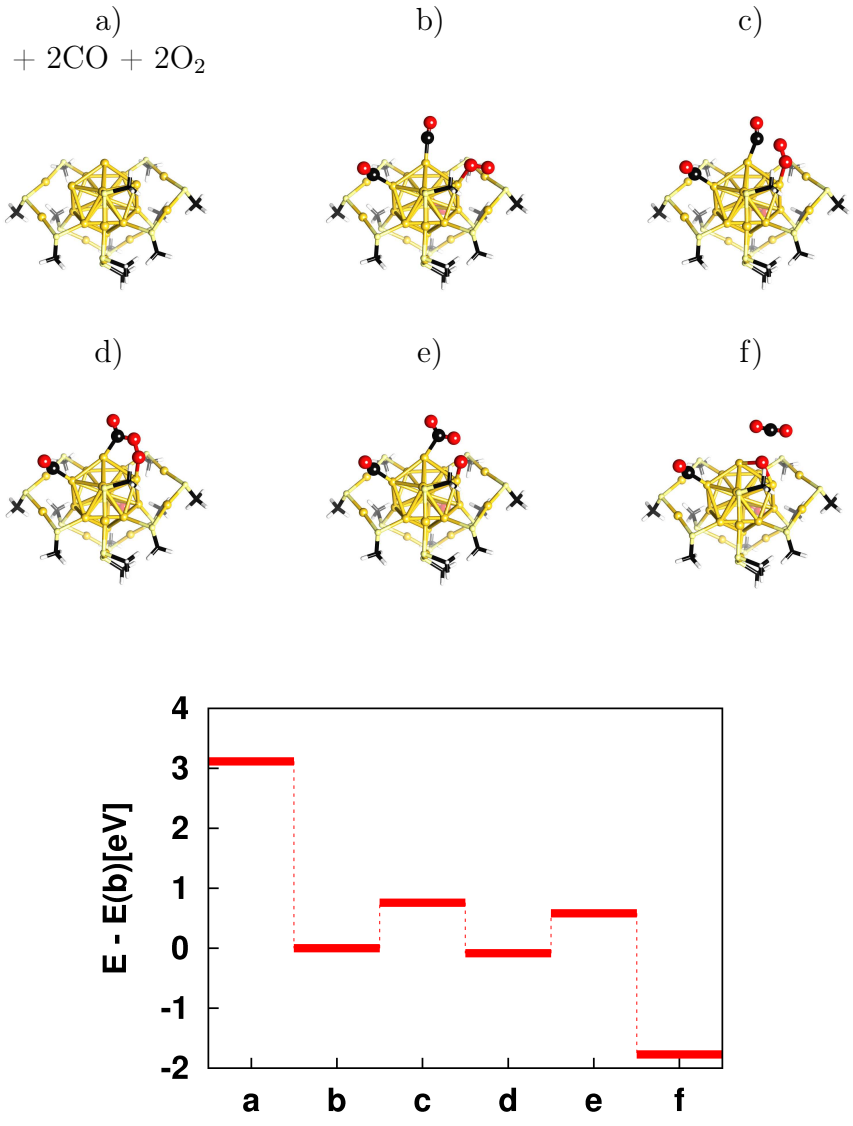

Figure 3.21: The energy landscape and the configurations for the important intermediate metastable minima and transition states in the Step 1 in the L-H reaction for the "10"-electron systems.

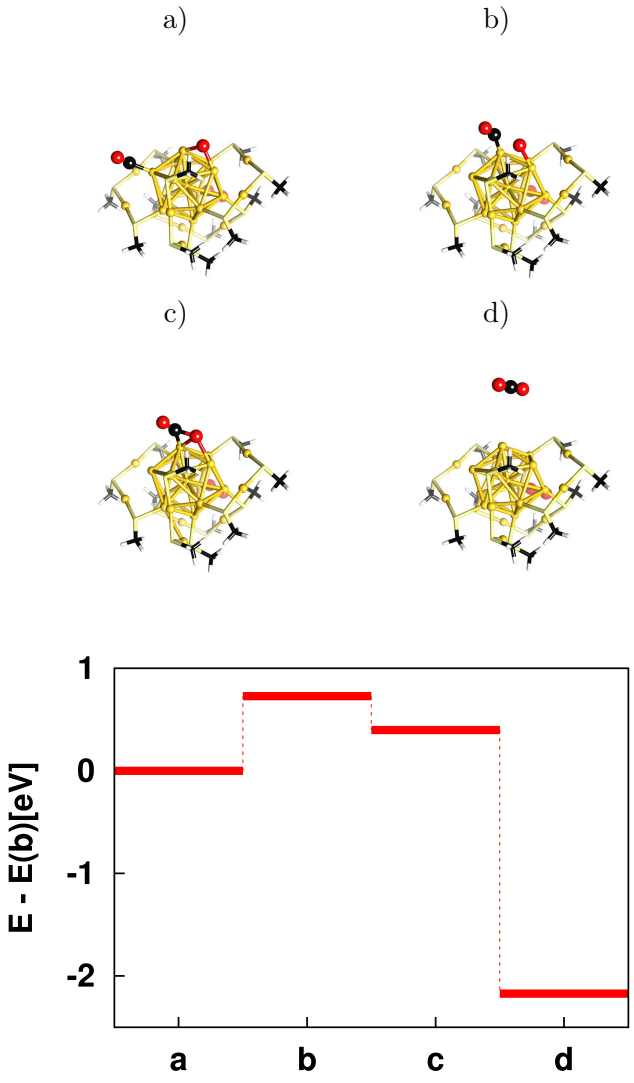

Figure 3.22: The energy landscape and the configurations for the important intermediate metastable minima and transition states in the Step 2 in the L-H reaction for the "10"-electron systems.

Table 3.2: The charge distribution in the "10"-electron cluster between CO, O_2 molecules, the core and the remaining ligands. The unit of charge is $|e|$.

	$[Au_{21}(SR)_{12}\text{-}O_2]^-$	$[Au_{21}(SR)_{12}\text{-}2O_2]^-$	$[Au_{21}(SR)_{12}\text{-}2O_2\text{-}2(CO)_2]^-$
$(O_2)_I$		-0.48	-0.47
$(O_2)_{II}$	-0.57	-0.57	-0.54
$(CO)_I$			-0.05
$(CO)_{II}$			-0.05
ligands	-0.67	-0.50	-0.60
core	0.24	0.55	0.72

the opposite side of the core (see Figure 3.18). Again, the core transfers charge a of 0.5 |e| to each oxygen molecule and activates them to the superoxo state with O-O distance of 1.30 Å. Distance between CO and O_2 is gradually reduced until a covalent C-O bond is formed, and the reaction barrier of 0.7 eV is found at 2.01 Å. The second transition of 0.6 eV is associated with the C-Au bond breaking. Figure 3.22 displays the remaining oxygen atom and CO molecule, which lead to the formation of another CO_2. Breaking the C-Au and O-Au bonds is associated with the calculated energy barrier of 0.7 eV. After this step, the three Au sites in the cluster are exposed and available for the next LH cycle.

Table 3.2 lists the charge distribution in the "10"-electron cluster between the CO and O_2 molecules, the Au_{13} core, and the remaining $Au_2(SR)_3$ ligands. Bader analysis indicates a transfer of a 0.5 |e| to each O_2 molecule. Moreover, $(O_2)_{\mathrm{I}}$ adsorbed on the three-fold exposed area is less negative than $(O_2)_{\mathrm{II}}$ adsorbed on the opposite side of the core, and the core transfers 0.48 |e| and 0.57 |e| to $(O_2)_{\mathrm{I}}$ and $(O_2)_{\mathrm{II}}$, respectively. In addition, the core becomes more positive, when all the exposed gold atoms are occupied by CO and O_2 molecules.

4 Summary and Outlook

In this thesis, the catalytic properties of small bare gold clusters as well as the electronic structure and chemical properties of thiolate-protected gold clusters and thiolated noble metal complexes were studied.

It was shown that the special "core-shell" structural motif of the $Au_{25}(SR)_{18}^{-1}$ cluster provides a framework for chemical modifications either of the core or of the ligand-shell quite independently. Doping the cluster by palladium impurity, in the well-defined core or in the protecting ligand shell changes the count of shell electrons in the metal core. In addition, the presence of strongly electron withdrawing groups in the ligand shell changes the charge distribution of the nanoparticle mainly inside the ligand shell without disturbing the delocalized states of the metallic core. Moreover, the results suggest that ionization potential of the cluster might be controlled by the number of the exchanged electron withdrawing ligands. The investigation of the dimers that were made from the "magic" clusters contributes to a better understanding of the intercluster interaction, which might lead to novel nano-material engineering, such as extended systems of chains or ordered networks with well-defined electronic, optical and magnetic properties. The comparative analysis of thiolated noble metal polymers $(MeSM)_x$, where $x \leq 12$, Me is methyl and M = Cu, Ag, Au; reveals that the metal-thiolate bonds are sterically flexible, i.e. ring-like, helix-like or catenane-like complexes are energetically competitive among the homoleptic complexes with dominantly covalent bond in the gold-thiolate and ionic bond in the copper-thiolate polymers.

The catalytic activity of small neutral gold clusters was studied through several reaction pathways for both the H_2O_2 and H_2O formation. The relative weight of the competing channels may depend on the size of the Au cluster, and both metadynamic and constrained MD simulations show significant fluxionality of the Au cluster during the course of the reaction. Activation of ligand-protected gold clusters can be obtained by partial removal of the protective layer, that makes the electropositive species which can bind and reduce dioxygen and catalyse ambient CO oxidation reactions.

Finally, few open issues still remain unresolved and some future perspectives motivate for further discussions. One of the unexplained subjects is the existence of a linear relationship between the experimentally observed intensity of the near-infrared luminescence and the number of electron-withdrawing ligands of $Au_{25}(SR)_{18}^{-}$. In addition, understanding of the factors that contribute to the relative energy differences of ferromagnetic and antiferromagnetic ordering in one or two-dimensional systems built

out of $MnAu_{24}$ units is crucial for a design of systems with tunable magnetic properties. Finally, the catalytic properties of thiolate protected clusters can be drastically affected by impurities. Thus, mixing (for example) palladium in the ultra-small gold core might improve the selectivity of oxidation reactions.

References

[1] P.L. Bernstein. *The power of gold: the history of an obsession.* Wiley and Sons, Inc, England, 2004.

[2] D.E. Bergeron, P.J. Roach, A.W. Jr. Castleman, N.O. Jones, and S.N. Khanna. *Science*, 307:231–235, 2005.

[3] S.A. Claridge, A.W. Castleman, S.N. Khanna, C.B. Murray, A. Sen, and P.S. Weiss. *Acs. Nano.*, 3:244–255, 2009.

[4] M.W. Heaven, A. Dass, P.S. White, K.M. Holt, and R.W. Murray. *J. Am. Chem. Soc.*, 130:3754–3755, 2008.

[5] M. Zhu, C.M. Aikens, F.J. Hollander, G.C. Schatz, and R. Jin. *J. Am. Chem. Soc.*, 130:5883–5885, 2008.

[6] P.D. Jadzinsky, G. Calero, C.J. Ackerson, D.A. Bushnell, and R.D. Kornberg. *Science*, 318:430, 2007.

[7] Philip Ball. Golden wonder. *Nat. Mat.*, 6:927, 2007.

[8] Y. Negishi, K. Nobusada, and T. Tsukuda. *J. Am. Chem. Soc.*, 127 (14):5261–5270, 2005.

[9] H. Grönbeck, M. Walter, and H. Häkkinen. *J. Am. Chem. Soc.*, 128:10268–10275, 2006.

[10] P. Pyykkö. *Chem. Soc. Rev.*, 37, 2008.

[11] R.M.Drezler andE.K.U. Gross. *Density Functional Theory. An Approximation to the Many-Body Problem.* Springer-Verlag, 1990.

[12] Robert van Leeuwen. *Density Functional Theory and its Applications in Nanoscience.* Lecture Notes. University of Jyväskylä, 2008.

[13] P. Hohenberg and W. Kohn. *Phys. Rev.*, 136:B864, 1964.

[14] W. Kohn and L.J. Sham. *Phys. Rev.*, 140:1133, 1965.

[15] http://nobelprize.org/nobel_prizes/lists/1998.html, 1998.

[16] D. P. Chong, O. V. Gritsenko, and E. J. Baerends. *J. Chem. Phys.*, 116:5, 2002.

[17] J.P. Perdew and K. Schmidt. *Density Functional Theory and Its Application to Materials*. V. Van Doren, C. Van Alsenoy, and P. Geerlings(AIP, Meliville, NY), 2001.

[18] P. Zeische, S. Kurth, and J.P. Perdew. *Comp. Mat. Sc.*, 11:122–127, 1998.

[19] John P. Perdew, Kieron Burke, and Matthias Ernzerhof. Generalized gradient approximation made simple. *Phys. Rev. Lett.*, 77:3865, 1996.

[20] Y. Zhang, W.Pan, and W.Yang. *J. Chem. Phys.*, 107:7921, 1997.

[21] D.C. Patton and M.R. Pederson. *Phys. Rev. A*, 56:R2495, 1997.

[22] D.C. Patton, D.V. Porezag, and M.R. Pederson. *Phys. Rev. B*, 55:7454, 1997.

[23] J.P. Perdew and S. Kurth. *Density Functionals for Non-Relativistic Coulomb Systems*. Lecture Notes in Physics. Springer, Berlin, 1998.

[24] U. von Barth. *Physica Scripta*, T109:9, 2004.

[25] J. Tao, J. P. Perdew, G. E. Scuseria, and V. N. Staroverov. *Prys. Rev. Lett.*, 91:146401, 2003.

[26] J. Tao, V. N. Staroverov, G. E. Scuseria, and J. P. Perdew. *Prys. Rev. A*, 77:012509, 2008.

[27] M. Born and R. Oppenheimer. *Ann. Phys.*, 84:457, 1927.

[28] C. Eckart. *Phys. Rev.*, 47:552, 1935.

[29] http://www.cpmd.org.

[30] R. Car and M. Parrinello. *Phys. Rev. Lett.*, 55:2471, 1985.

[31] N. Troullier and Jos Luriaas Martins. *Phys. Rev. B*, 43:1993–2006, 1991.

[32] D. Vanderbilt. *Phys. Rev. B*, 41:7892–7895, 1990.

[33] P. Blöchl. *Phys. Rev. B*, 50:17953, 1994.

[34] D. R. Hamann, M. Schlüter, and C. Chiang. *Phys. Rev. Lett.*, 43:1494–1497, 1979.

[35] Jaakko Akola. *DFT in Practice: Computational Aspects*. Lecture Notes. Pseudopotentials & PAW. University of Jyväskylä, 2009.

[36] J.J. Mortensen, L.B. Hansen, and K.W. Jacobsen. *Phys. Rev. B*, 71:035109, 2005.

[37] D. Sheppard, R. Terrell, and G. Henkelman. *J. Chem. Phys.*, 128:134106, 2008.

[38] R. A. Olsen, G. J. Kroes, G. Henkelman, A. Arnaldsson, and H. Jónsson. *J. Chem. Phys.*, 121:9776–9792, 2004.

[39] G. Henkelman, G. Jóhannesson, , and H. Jónsson. *Methods for Finding Saddle Points and Minimum Energy Paths*. Kluwer Academic Publishers.

[40] C. Choi and R. Elber. *J. Chem. Phys.*, 94:751, 1991.

[41] H. Jónsson, G. Mills, and W. Jacobsen. *Nudged Elastic Band Method for Finding Minimum Energy Paths of Transitions*. 1998.

[42] G. Henkelman and H. Jónsson. *J. Chem. Phys.*, 113:9978, 2000.

[43] G. Henkelman and H. Jónsson. *J. Chem. Phys.*, 111:7010, 1999.

[44] G. Henkelman, Uberuaga, and H. Jonsson. *J. Chem. Phys.*, 113, 2000.

[45] A. Szabo and N.S. Ostlund. *Modern Quantum Chemistry*. Dover (Mineola, NY), 1982.

[46] R. F. W. Bader. *Atoms in Molecules - A Quantum Theory*. Oxford University Press, Oxford, 1990.

[47] Matthew R. Wiseman, Patsy A. Marsh, Peter T. Bishop, Brian J. Brisdon, and Mary F. Mahon. *J. Am. Chm. Soc.*, 122:12598–12599, 2000.

[48] Chi-Ming Che Stephen Sin-Yin Chui, Rong Chen. *Angew. Chem. Int. Ed*, 45:1621–1624, 2006.

[49] R. Bau. *J. Am. Chem. Soc.*, 120:9380, 1998.

[50] C. F. Shaw. *Chem. Rev.*, 99:2589, 1999.

[51] N. Shao, Y. Pei, Y. Gao, and X. C. Zeng. *J. Phys. Chem. C*, 113:629, 2009.

[52] R.L. Donkers, D. Lee, and R.W. Murray. *Langmuir*, 20:1945–1952, 2004.

[53] Z. Wu, J. Suhan, and R. Jin. *J. Mater. Chem.*, 19:622–626, 2009.

[54] M. Walter, J. Akola, O. Lopez-Acevedo, P. D. Jadzinsky, G. Calero, C. J. Ackerson, R. L. Whetten, H. Grönbeck, and H. Häkkinen. *Proc. Natl. Acad. Sci*, 105:9157, 2008.

[55] J. Akola, M. Walter, H. Häkkinen, and H. Grönbeck. *J. Am. Chem. Soc.*, 130:3756, 2008.

[56] H. Häkkinen. *Chem. Soc. Rev.*, 37:1847, 2008.

[57] H. Häkkinen, M. Walter, and H. Grönbeck. *J. Phys. Chem. B*, 110:9927, 2006.

[58] J. Akola, M. Walter, R.L. Whetten, H. Häkkinen, and H.J. Grönbeck. *J. Am. Chem. Soc.*, 130:2008, 3756.

[59] P. Jadzinsky, G. Calero, C.J.Ackerson, D.A.Bushnell, and R.D.Kornberg. *Science*, 318:430, 2007.

[60] C. Fields-Zinna, M.Crowe, A. Dass, J.E.F. Weaver, and R.W.Murray. *Langmuir*, 25:7704–7710, 2009.

[61] R. Guo and R.W. Murray. *J. Am. Chem. Soc.*, 127:12140–12143, 2005.

[62] S.N. Khanna and P. Jena. *Phys. Rev. Lett.*, 69:1664–1667, 1992.

[63] W. Peter Wuelfing, Francis P. Zamborini, Allen C. Templeton, Xingu Wen, Heidi Yoon, and Royce W. Murray. *Chem. Mater.*, 13:87–95, 2001.

[64] F.P. Zamborini; M.C. Leopold; J.F. Hicks; P.J. Kulesza; M.A. Malik; R.W. Murray. *J. Am. Chem. Soc.*, 124:8958–8964, 2002.

[65] J.F. Hicks, F.P. Zamborini, and R.W. Murray. *J. Phys. Chem. B.*, 106:7751–7757, 2002.

[66] J.F. Hicks, F.P. Zamborini, A.J. Osisek, and R.W. Murray. *J. Am. Chem. Soc.*, 123:7048–7053, 2001.

[67] J.U. Reveles, P.A. Clayborne, A.C. Reber, S.N. Khanna, K. Pradhan, P. Sen, and M.R. Pederson. *Nature Chemistry*, 1:310 – 315, 2009.

[68] D. Jiang and R.L. Whetten. *Phys. Rev. B*, 113:16983, 2009.

[69] J. J Berzelius. *Royal Swedish Academy of Sciences*, 1835.

[70] B. Lindstrom and L.J. Pettersson. *Cat. Tech.*, 7:130–138, 2003.

[71] Encyclopedia Britannica.

[72] G. C. Bond. *Cat. Tod.*, 72:5–9, 2002.

[73] G.A. Ozin. *Acc. Chem. Res.*, 21:10, 1977.

[74] R.E. Leuchtner, A.C. Harms, and A.W.Jr. Castleman. *J. Chem. Phys. 91*, 91:2753–2754, 1989.

[75] A.W.Jr. Castleman and S.N. Khanna. *J. Phys. Chem. C*, 113:2664–2675, 2009.

[76] M. Haruta. *Cat. Tod.*, 36:153–166, 1997.

[77] J.A. Bokhoven, C. Louis, J.T. Miller, M. Tromp, O.V. Safonova, and P. Glatzel. *Angew. Chem. Int. Ed.*, 45:4651–4654, 2006.

[78] A. Sanchez, S. Abbet, U. Heiz, W.-D. Schneider, H. Häkkinen, R. N. Barnett, and Uzi Landman. *J. Phys. Chem. A*, 103:9573, 1999.

[79] H. Häkkinen, S. Abbet, A. Sanchez, U. Heiz, and U. Landman. *Angew. Chem. Int. Ed.*, 42:1297, 2003.

[80] B. Yoon, H. Häkkinen, U. Landman, A. Wörz, J.-M. Antonietti, S. Abbet, K. Judai, and U. Heiz. *Science*, 307:403, 2005.

[81] U. Heiz and U. Landman. *Nanocatalysis*. Springer, 2007.

[82] M.M. Schubert, S. Hackenberg, A.C. van Veen, M. Muhler, V.Plzak, and R.J. Behm. *J. of. Catal.*, 197:113–122, 2001.

[83] M.Dat, M.Okumura, S. Tsubota, and M. Haruta. *Angew. Chem. Int. Ed.*, 43:2129–213, 2004.

[84] D. A. H. Cunningham, W. Vogel, H. Kageyama, S. Tsubota, and M. Haruta. *J. Catal.*, 177, 1998.

[85] H. Liu, A. I. Kozlov, A. P. Kozlova, T. Shido, and Y. Iwasawa. *Phys. Chem. Chem. Phys.*, 1:2851, 1999.

[86] https://wiki.fysik.dtu.dk/gpaw.

[87] C. Sichela, P. Fernández-Ibáñeza, M. de Carac, and J. Telloc. *Water Research*, 43:1841–1850, 2009.

[88] W.T. Hess, J.I. Kroschwitz, and M. Howe-Grant. *Kirk-Othmer Encyclopedia of Chemical Technology 4th ed.*, volume 13. Wiley, New York, Oxford, 1995.

[89] V. Hulea, F. Fajula, and J. Bousquet. *J. Catal.*, 189:179, 2001.

[90] P. Landon, P.J. Collier, A.J. Papworth, C.J. Kiely, and G.J. Hutchings. *Chem. Comm.*, page 2058, 2002.

[91] B.E. Solsona, J.K. Edwards, P. Landon, A.F. Carley, A. Herzing, C.J. Kiely, and G.J. Hutchings. *Chem. Mater.*, 55:2689, 2006.

[92] J.K. Edwardsa, A. Thomas, A.F. Carley, A.A. Herzing, C.J. Kiely, and G.J. Hutchings. *Green Chem.*, 10:388, 2008.

[93] J.H. Lundsford. *J. Cat.*, 216:455–460, 2003.

[94] C. Stampfl and M. Scheffler. *Phys. Rev. Lett.*, 78:1500, 1997.